

## Low-Frequency Variability in Shallow-Water Models of the Wind-Driven Ocean Circulation. Part II: Time-Dependent Solutions\*

ERIC SIMONNET<sup>+</sup>

*Laboratoire de Mathématiques, Université Paris-Sud, Orsay, France*

MICHAEL GHIL<sup>#</sup> AND KAYO IDE

*Department of Atmospheric Sciences, and Institute of Geophysics and Planetary Physics, University of California, Los Angeles, Los Angeles, California*

ROGER TEMAM

*Laboratoire de Mathématiques, Université Paris-Sud, Orsay, France, and Department of Mathematics, Indiana University, Bloomington, Indiana*

SHOUHONG WANG

*Department of Mathematics, Indiana University, Bloomington, Indiana*

(Manuscript received 12 March 2001, in final form 19 September 2002)

### ABSTRACT

The time-dependent wind-driven ocean circulation is investigated for both a rectangular and a North Atlantic-shaped basin. Multiple steady states in a 2½-layer shallow-water model and their dependence on various parameters and other model properties were studied in Part I for the rectangular basin. As the wind stress on the rectangular basin is increased, each steady-state branch is destabilized by a Hopf bifurcation. The periodic solutions that arise off the subpolar branch have a robust subannual periodicity of 4–5 months. For the subtropical branch, the period varies between sub- and interannual, depending on the inverse Froude number  $F_2$  defined with respect to the lower active layer's thickness  $H_2$ . As  $F_2$  is lowered, the perturbed-symmetric branch is destabilized baroclinically, before the perturbed pitchfork bifurcation examined in detail in Part I occurs. Transition to aperiodic behavior arises at first by a homoclinic explosion off the isolated branch that exists only for sufficiently high wind stress. Subsequent global and local bifurcations all involve the subpolar branch, which alone exists in the limit of vanishing wind stress. Purely subpolar solutions vary on an interannual scale, whereas combined subpolar and subtropical solutions exhibit complex transitions affected by a second, subpolar homoclinic orbit. In the latter case, the timescale of the variability is interdecadal. The role of the global bifurcations in the interdecadal variability is investigated. Numerical simulations were carried out for the North Atlantic with earth topography-5 minute (ETOPO-5) coastline geometry in the presence of realistic, as well as idealized, wind stress forcing. The simulations exhibit a realistic Gulf Stream at 20-km resolution and with realistic wind stress. The variability at 12-km resolution exhibits spectral peaks at 6 months, 16 months, and 6–7 years. The subannual mode is strongest in the subtropical gyre; the interannual modes are both strongest in the subpolar gyre.

### 1. Introduction

Part I of this study (Simonnet et al. 2003) was devoted to an investigation of our 2½-layer shallow-water (SW)

model's steady-state solutions. We studied therein the branching structure of these solutions when several parameters were varied. These included the wind stress intensity  $\sigma$ , the inverse Froude number  $F_2$  of the lower active layer, and the interface Rayleigh viscosity coefficient  $\mu_1$ . The model's multiple steady states, two stable and one unstable, arise from a perturbed pitchfork bifurcation that is robust with respect to changes in spatial resolution and the degree of north–south asymmetry in the time-constant wind stress. The basic bifurcation diagram appears in Fig. 2 of Part I, where the definition of the three branches—subpolar, perturbed symmetric, and subtropical—is also given.

Multiple steady flows, however, are only the first step

\* Institute of Geophysics and Planetary Physics Publication Number 5744.

<sup>+</sup> Current affiliation: Institut Non-Linéaire de Nice, Valbonne, France.

<sup>#</sup> Current affiliation: Ecole Normale Supérieure, LMD, CNRS, Paris, France.

*Corresponding author address:* Dr. Eric Simonnet, Institut Non-Linéaire de Nice (INLN), UMR 6618, CNRS 1361, route des Lucioles, 06560 Valbonne, France.

E-mail: eric.simonnet@inln.cnrs.fr

on the successive-bifurcation road to explaining the observed irregularities (Ruelle and Takens 1971; Eckmann 1981) of planetary, rotating flows (Ghil and Childress 1987). We now focus in Part II (the present paper) on the dynamics that leads to time-dependent solutions and the occurrence of low-frequency variability. The further steps taken on this road for the present model are through Hopf bifurcations, as well as global bifurcations.

Homoclinic and heteroclinic bifurcations do not arise—like saddle-node, pitchfork, or Hopf bifurcation—through the nonlinear saturation of a steady-state solution's linear instabilities. Instead, they are due to behavior that is global, rather than local, in a system's phase space; to wit, the stable and unstable manifolds of one (homoclinic reconnection) or more (heteroclinic connections) steady solutions become connected. The role of such global bifurcations in transition to irregular behavior for a rotating, stratified flow was first pointed out by Lorenz (1963). More recently, they also played an important role in generating low-frequency variability in simpler models of the wind-driven double-gyre circulation (Meacham 2000; Chang et al. 2001; Nadiga and Luce 2001).

Section 2 is devoted to the study of the Hopf bifurcations that lead to limit cycles in the rectangular-basin version of the model. In section 3, we describe the transitions to aperiodic behavior, as well as the phenomenology of low-frequency variability. This variability is examined for a geometry and wind stress that approximate fairly closely the North Atlantic basin in section 4, where it is also compared with observations. Concluding remarks follow in section 5. Preliminary results of this investigation were reported by Simonnet (1998) and Simonnet et al. (1998).

## 2. Oscillatory instabilities and limit cycles

The stability transfer from stationary to periodic solutions occurs here through *supercritical* Hopf bifurcation, as found already in simpler double-gyre models by Jiang et al. (1995), Speich et al. (1995), and Dijkstra and Katsman (1997), among others. That is, stable periodic solutions of gradually increasing amplitude are found as a parameter varies continuously; that is, the amplitude of the stable limit cycle starts out equal to zero at the bifurcation point itself and increases monotonically up to a finite value.

A detailed study of the linear stability problem about the subpolar branch of solutions in Fig. 2 of Part I yields the diagram in Fig. 1 here. To obtain it, we computed the leading modes of the problem at different values of  $\sigma$  on either side of the Hopf bifurcation. The bifurcation point is defined by the value of  $\sigma$  for which a pair of complex eigenvalues crosses the imaginary axis. Other parameter values are equal to those given in Table 1, unless otherwise stated.

The first Hopf bifurcation for the subpolar branch of

solutions occurs at  $\sigma_{\text{HB}}^{(\text{pol})} \equiv \sigma_1^{(\text{pol})} = 2.717 \times 10^{-3}$ , where the first mode, labeled 1 in the figure, crosses the imaginary axis. The value  $\omega_0 = 0.4909$  of the imaginary part at which this happens gives a period for the small-amplitude perturbation at nearby  $\sigma$  values of  $T_1^{(\text{pol})} = 2\pi/\omega_0 = 148$  days. This theoretical period coincides with the actual period of solutions computed for this branch by forward integration of the model equations, Eqs. (4) in Part I, as long as we are close enough to the Hopf bifurcation (not shown).

A striking property of the destabilization process is the occurrence of a very small number of unstable modes: we obtained only four unstable modes, even for fairly large values of  $\sigma$ . The first two modes (1 and 2) evolve slowly and regularly with  $\sigma$  and appear well before the Hopf bifurcation. The second mode becomes unstable at  $\sigma_2^{(\text{pol})} = 2.905 \times 10^{-3}$ . The following two modes (3 and 4) appear quite suddenly at  $\sigma_3^{(\text{pol})} = 3.220 \times 10^{-3}$  and  $\sigma_4^{(\text{pol})} = 3.750 \times 10^{-3}$ . They change much more rapidly as  $\sigma$  changes than the first two modes.

We did not plot here the other eigenvalues; they change very little as  $\sigma$  increases and are not expected to cross the imaginary axis, even for substantially larger  $\sigma$  values. The ordering of internal modes of variability is not a robust feature in our model: the mode labeled 2 may cross the imaginary axis before mode 1, depending on the parameter regime explored. However, the presence of these modes is very robust and they play an important role in the low-frequency dynamics of the flow (see also Dijkstra and Molemaker 1999).

To investigate the oscillatory instability that leads to periodic solutions, we compute the eigenvectors ( $\mathbf{w}_R$ ,  $\mathbf{w}_I$ ) associated with the pair of complex conjugate eigenvalues that crosses the imaginary axis at  $(\pm i\omega_0)$ . The time-periodic linear transition state is given by  $\Psi(t) = \cos(\omega_0 t)\mathbf{w}_R - \sin(\omega_0 t)\mathbf{w}_I$  for  $0 \leq t \leq T$ . For greater dynamical insight, we plot the streamfunction anomaly fields  $\psi_1 = F_1 h'_1 + F_2 h'_2$  and  $\psi_2 = \gamma F_1 h'_1 + F_2 h'_2$  in the upper and lower layer, respectively. These fields, unlike the thickness eigenvectors  $h'_1$  and  $h'_2$ , are in geostrophic equilibrium [see Part I Eqs. (11) and (16)] and help us detect phase shifts between the two layers.

The imaginary and real part of the streamfunction eigenvectors is plotted below the panels that show the evolution of the eigenvalues' corresponding part. The imaginary part  $\mathbf{w}_I$  corresponds to  $t = -T/4$  and the real part  $\mathbf{w}_R$  to  $t = 0$ . These anomaly patterns appear in Fig. 1 for the first and second Hopf bifurcation off the subpolar branch, at  $\sigma_1^{(\text{pol})}$  and  $\sigma_2^{(\text{pol})}$ , respectively. We also computed, when Eqs. (4) of Part I are integrated forward in time, the actual differences between the instantaneous fields and the limit cycle's mean state: the patterns so obtained (not shown) are essentially the same as the time-periodic linear transition states plotted in Fig. 1 here.

These periodic disturbances are predominantly barotropic for both the subpolar (Fig. 1) and subtropical (Fig. 2) branches. The first two modes to become un-

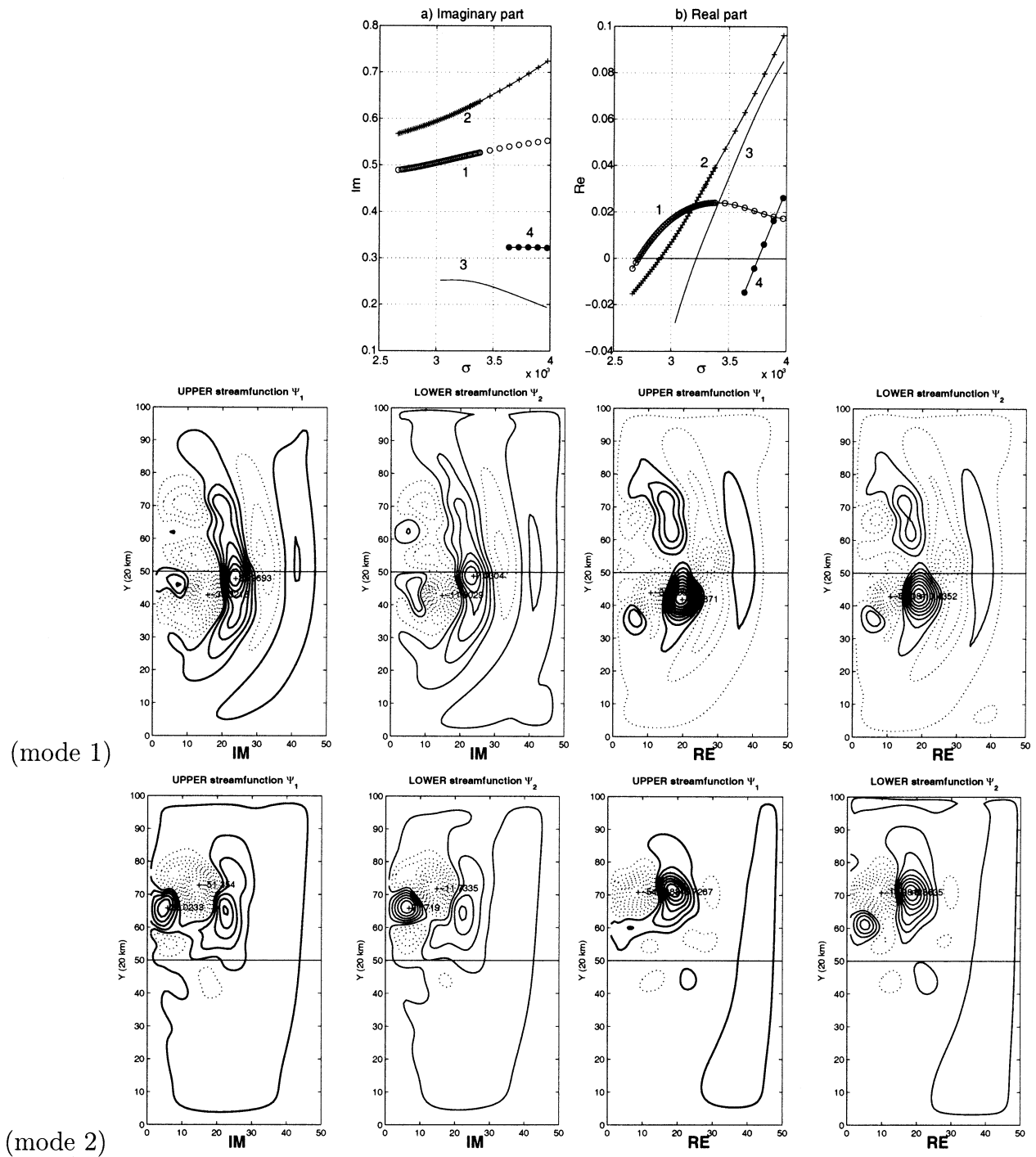


FIG. 1. Eigenvalues and eigenmodes for the linear stability problem on the subpolar solution branch. The evolution of the eigenvalues as a function of the wind stress intensity  $\sigma$ , for  $2.664 \times 10^{-3} \leq \sigma \leq 4.120 \times 10^{-3}$ , is shown in the two uppermost panels: imaginary part (left) and real part (right). The first four unstable modes are labeled in the order in which their real parts become positive. The streamfunctions  $\psi_1$  and  $\psi_2$  of the first two eigenmodes are shown in the two sets of four panels below (imaginary part to the left, i.e., at  $t = -T/4$ , and real part to the right, i.e., at  $t = 0$ ).

TABLE 1. Reference values of the model's nondimensional parameters. See section 2a of Part I for a detailed definition of the parameters,  $\sigma$  being the nondimensional intensity of the wind stress,  $\epsilon$  the Rossby number,  $\beta$  the nondimensional version of the Coriolis parameter's meridional gradient,  $E$  the Eckman number,  $\mu_1$  and  $\mu_2$  the Rayleigh viscosity coefficients, and  $F_1$  and  $F_2$  the inverse Froude numbers; subscripts 1 and 2 designate the model's upper and lower active layers.

Parameter	$\sigma$	$\epsilon$	$\beta$	$E$	$\mu_1$	$\mu_2$	$F_1$	$F_2$
Value	$0.25 \times 10^{-2}$	0.02	20	$0.6 \times 10^{-5}$	$10^{-3}$	$10^{-3}$	20	4.0

stable off the subpolar branch (see Fig. 1, modes 1 and 2) correspond to Rossby basin modes (cf. Sheremet et al. 1997; Chang et al. 2001) that propagate westward and interact with the jet or the subpolar recirculation cell. Mode 2 is, in fact, the same mode as the first unstable subpolar mode found by Speich et al. (1995). Its associated period, at  $\sigma_2^{(pol)}$ , is  $T_2^{(pol)} = 120$  days.

The first Hopf bifurcation off the subtropical branch occurs at  $\sigma_{HB}^{(ro)} \equiv \sigma_1^{(ro)} = 2.821 \times 10^{-3}$ , with a period of  $T_1^{(ro)} = 704$  days (1.92 yr). The corresponding oscillatory instability (Fig. 2, mode 1) is a barotropic gyre

mode that propagates southwestward. This mode has an elongated wave pattern distorted by the jet and by advection in the subtropical recirculation cell; its troughs and ridges are roughly lined up along a northwest-southeast direction (see also Jiang et al. 1995; Speich et al. 1995; Dijkstra and Katsman 1997; Chang et al. 2001).

Simonnet and Dijkstra (2002) have shown that this oscillatory mode originates from the merging of two zero-frequency modes, as one follows the asymmetric branch of solutions. These two modes are both nonoscillatory and they are responsible for the first pitchfork bifurcation and saddle-node bifurcation which occur off the symmetric branch in quasigeostrophic (QG) models. This spectral merging of zero-frequency modes explains the low-frequency behavior of the oscillatory gyre mode, as well as its key presence throughout a hierarchy of models of the double-gyre circulation. The physical mechanism responsible for this pervasive gyre mode is very similar to the one observed at the symmetry-breaking pitchfork bifurcation and involves a shear instability that feeds on the asymmetry of the flow.

The spatial pattern of mode 3 in Fig. 1 (not shown)

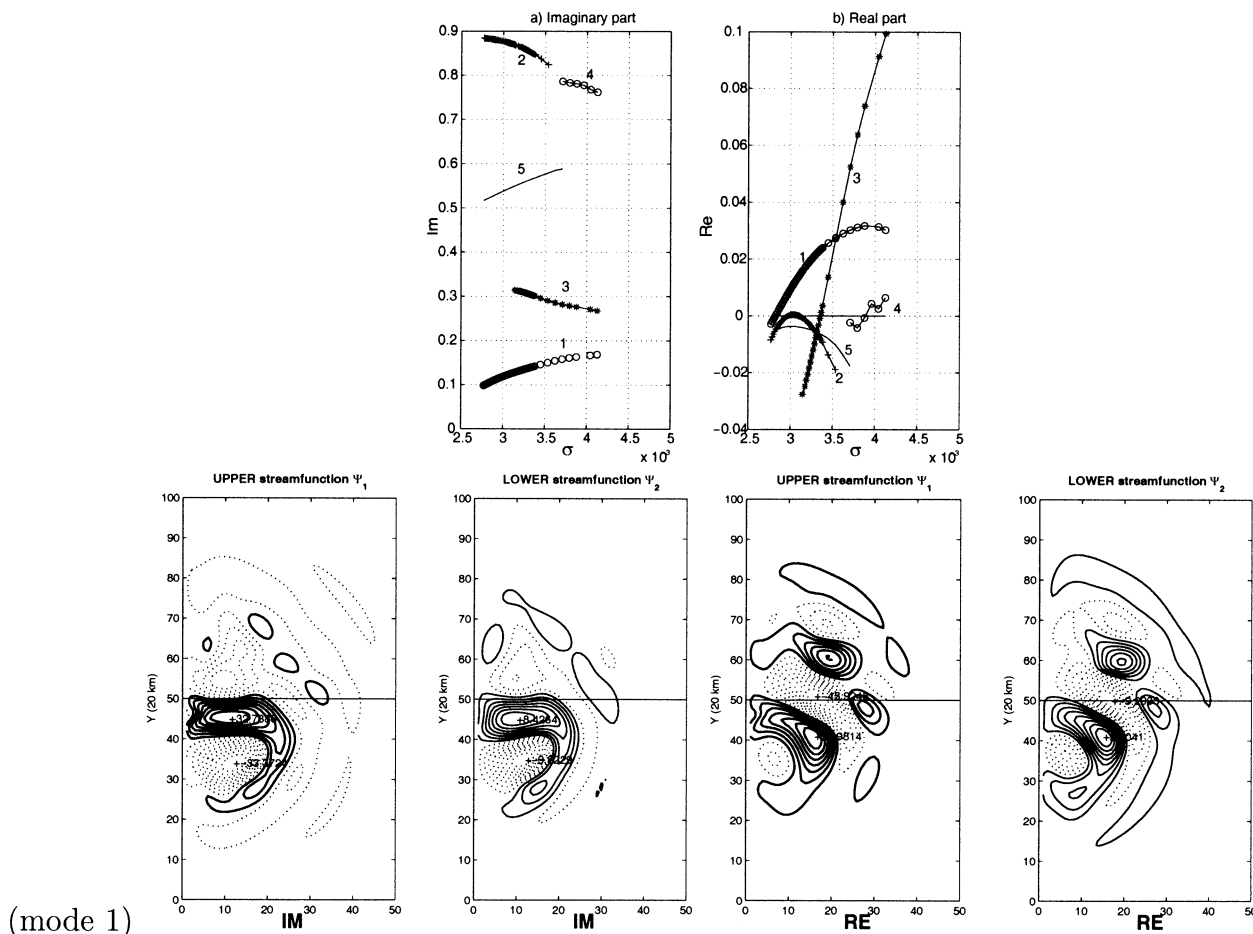


FIG. 2. As in Fig. 1 but for the subtropical branch and the streamfunction anomalies for mode 1.

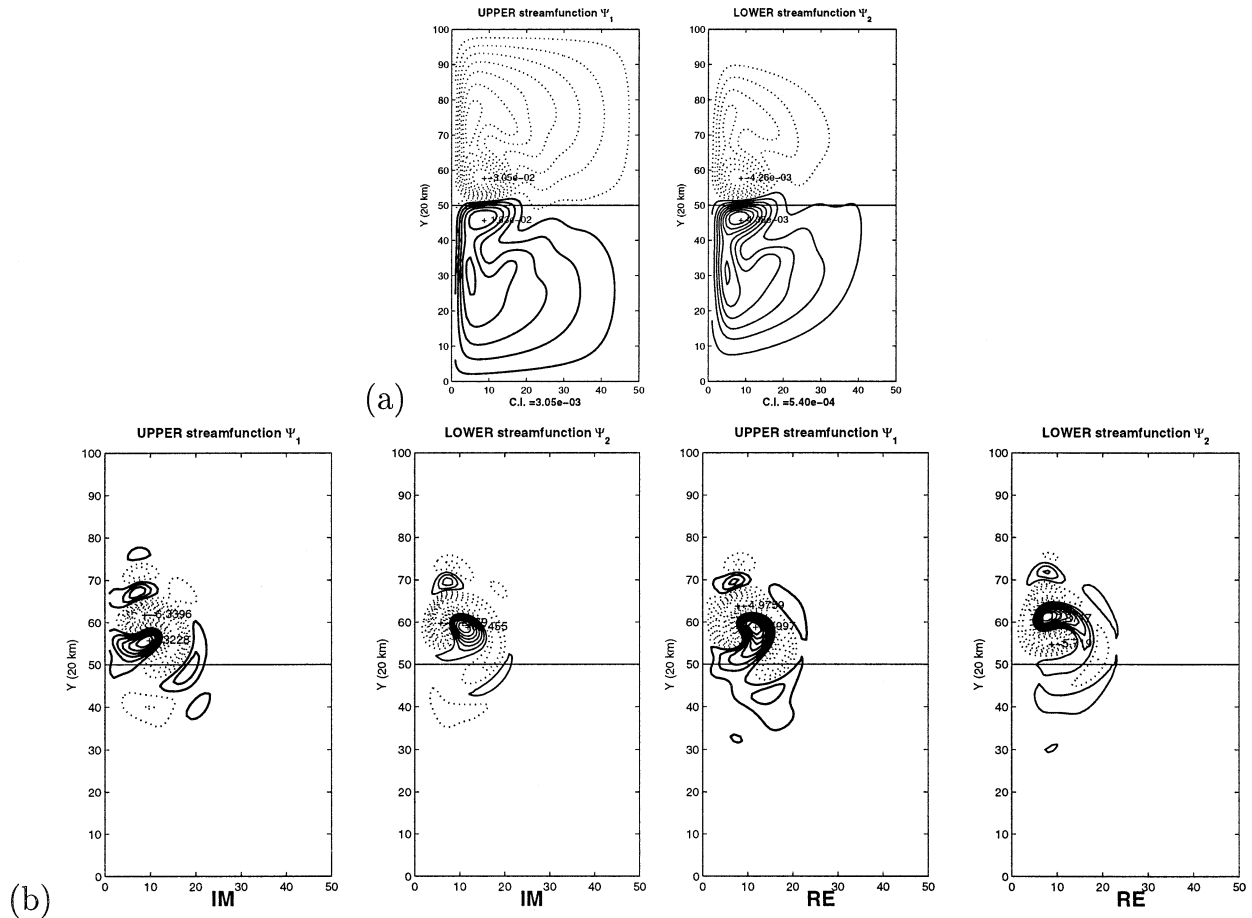


FIG. 3. Oscillatory instability off the subpolar branch for  $\sigma = 1.718 \times 10^{-3}$  and  $F_2 = 1.67077$ ; all other parameter values as in Fig. 6 of Part I (with  $\mu_1 \neq 0$ , i.e., as in that figure's lower panel). Total mean fields  $\Psi_1$  and  $\Psi_2$  are in the two upper panels and anomalies  $\psi_1$  and  $\psi_2$  are below. The period is  $T = 116$  days.

appears to be the (perturbed) mirror symmetric image of the subtropical gyre mode whose spatiotemporal pattern is shown in Fig. 2. These modes are important features of the double-gyre circulation since they are quite model independent, vary on an interannual timescale, and are in general more energetic than Rossby waves or mesoscale eddies.

Mode 2 in Fig. 2 (upper panel) crosses the imaginary axis at  $\sigma_2^{(ro)} = 2.97 \times 10^{-3}$  with a short period of 83 days; it does not influence the time-dependent solutions noticeably and becomes stable again at  $\sigma = 3.11 \times 10^{-3}$ . As  $\sigma$  is increased further, global bifurcations occur and start to affect the time-dependent behavior of model solutions.

The barotropic nature of the instabilities in Figs. 1 and 2 appears to be parameter dependent. We obtained a more pronounced baroclinic structure for the destabilizing mode shown in Fig. 3. The solution corresponding to this linearly unstable mode is represented by an open circle in the lower-left corner of the lower panel of Fig. 6 in Part I. The values of  $F_2$  and  $\sigma$  here differ from those in Figs. 2 and 3 (and in Table 1). This in-

stability occurs before the (perturbed) pitchfork bifurcation.

The mode shown in Fig. 3 exhibits a phase shift between the upper and lower layer of approximately  $T/4$  that is characteristic of baroclinic instabilities. The disturbances are centered on the cyclonic recirculation cell; they rotate cyclonically and, in doing so, make the vorticity in the recirculation zone vary. Dijkstra and Katsman (1997) found the same mode in their QG baroclinic model to arise from their second Hopf bifurcation. It only affects the strongest recirculation cell, which is the subpolar one in the present study. In the perfectly symmetric QG model, the two recirculation cells oscillate both in phase quadrature (see also Ghil et al. 2002b, for the relative ordering of this baroclinic, oscillatory instability, and the basically barotropic pitchfork bifurcation).

### 3. Low-frequency variability and aperiodic attractors

As the wind stress strength  $\sigma$  increases further, periodic solutions lose their stability and the model's be-

havior becomes irregular. In this regime, solutions exhibit more and more complex features as the number of vortices and their interactions with each other increases. Still, these temporally irregular and spatially complex solutions are expected to converge asymptotically to a finite-dimensional strange attractor (Ruelle and Takens 1971; Constantin et al. 1989; Temam 1998).

In geophysical fluid dynamics problems such as this one, the constraints imposed on the flow by rotation and stratification help maintain the attractor's number of dimensions rather low (Ghil and Childress 1987; Lions et al. 1997). This expectation is strengthened by the small number of unstable modes that arise well beyond the first Hopf bifurcation (see Fig. 1 and discussion there). Thus, a finite and not too large number of degrees of freedom should describe the asymptotic behavior of solutions that are already fairly chaotic in time and complex in space; see also Berloff and Meacham (1997) for the problem at hand.

For an intermediate range of  $\sigma$  values, we find three "local" attractors: two stable ones around the subtropical and the subpolar branch of steady states and one unstable one around the perturbed-symmetric branch (see Fig. 2 in Part I). For even larger values of  $\sigma$ , global bifurcations alter this picture further, so it is difficult to refer to local attractors: for instance, the dynamics near the isolated branch, which includes both the perturbed-symmetric and the subtropical branch, is governed by a single, global attractor past a critical value of  $\sigma$ . This is the subject of section 3a.

The subpolar attractors are more robust for increasing  $\sigma$ , as shown in section 3b. The two families of attractors, subpolar and subtropical-symmetric, eventually merge into one global attractor with complex transitions between the neighborhoods of the various branches. These phenomena are described in section 3c.

#### a. The isolated-branch attractors

The limit cycle near the first Hopf bifurcation on the subtropical branch is characterized by interannual periods, while the subpolar-branch one has subannual periods. The periods of the fully nonlinear solutions thus agree with the corresponding Hopf bifurcation periods obtained in section 4b of Part I (see also section 2 here). Speich et al. (1995) suggest that the difference in time-scale between the periodic solutions off the two branches is due to the different balances that prevail between the linear, dispersive terms, the nonlinear, advective ones, and the forcing terms in the case where the cyclonic versus the anticyclonic recirculation dominates. To their considerations we may add that, for the parameter range under study, baroclinicity—present in our model but not theirs—is not an important factor, at least when one is sufficiently close to the first Hopf bifurcation (see Figs. 1 and 2 and their discussion in the previous section).

To examine the behavior on the attractor for larger

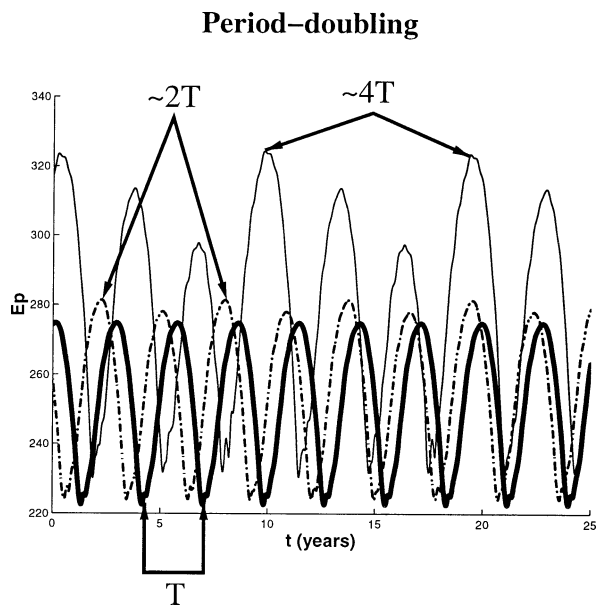


FIG. 4. Potential energy time series for three subtropical periodic solutions:  $\sigma = 2.871 \times 10^{-3}$  (period  $T = 2.88$  yr: heavy solid line),  $\sigma = 2.882 \times 10^{-3}$  (period  $2T$ : dashed line), and  $\sigma = 2.947 \times 10^{-3}$  (period  $4T$ : light solid line).

values of the wind stress parameter  $\sigma$ , we integrate forward in time Eqs. (4) of Part I over one century or so, and study the time series of kinetic and potential energy, as well as the normalized transport difference TD, given in Eqs. (8) and (25) of Part I, respectively. Two different kinds of periodic solutions appear as we increase  $\sigma$ . One starts out close to the first Hopf bifurcation with a period of  $T = 1.92$  yr. This period increases noticeably as  $\sigma$  varies from  $\sigma_1^{(no)} = 2.821 \times 10^{-3}$  to  $\sigma = 2.871 \times 10^{-3}$ , where it becomes  $T = 2.83$  yr. The corresponding solution is a gyre mode that is characterized by a relaxation oscillation (Simonnet and Dijkstra 2002).

At  $\sigma = 2.882 \times 10^{-3}$ , the primary period is doubled to  $T = 5.75$  yr (see Fig. 4). The oscillation is now characterized by two cycles with slightly different amplitudes. Such a transition is characteristic of a so-called flip or period-doubling bifurcation, which occurs within the interval  $[2.871 \times 10^{-3}, 2.882 \times 10^{-3}]$ . In such a bifurcation, a Floquet exponent of the system linearized about the primary limit cycle crosses the unit circle; this corresponds geometrically to a fixed point of the second iterate of the Poincaré map that is induced by the primary limit cycle (Guckenheimer and Holmes 1990).

Direct Floquet analysis for problems in atmospheric (Strong et al. 1995) and coupled ocean-atmosphere (Jin et al. 1996) models has been performed for a number  $n$  of grid point or spectral variables  $O(10^2-10^3)$ . To do so for a problem of the present size, with  $n = O(10^4)$  would be numerically very challenging. Our evidence for a flip bifurcation is therefore only indirect at this point. Further period-doubling bifurcations occur past  $\sigma = 2.921 \times 10^{-3}$ . One thus observes a limit cycle

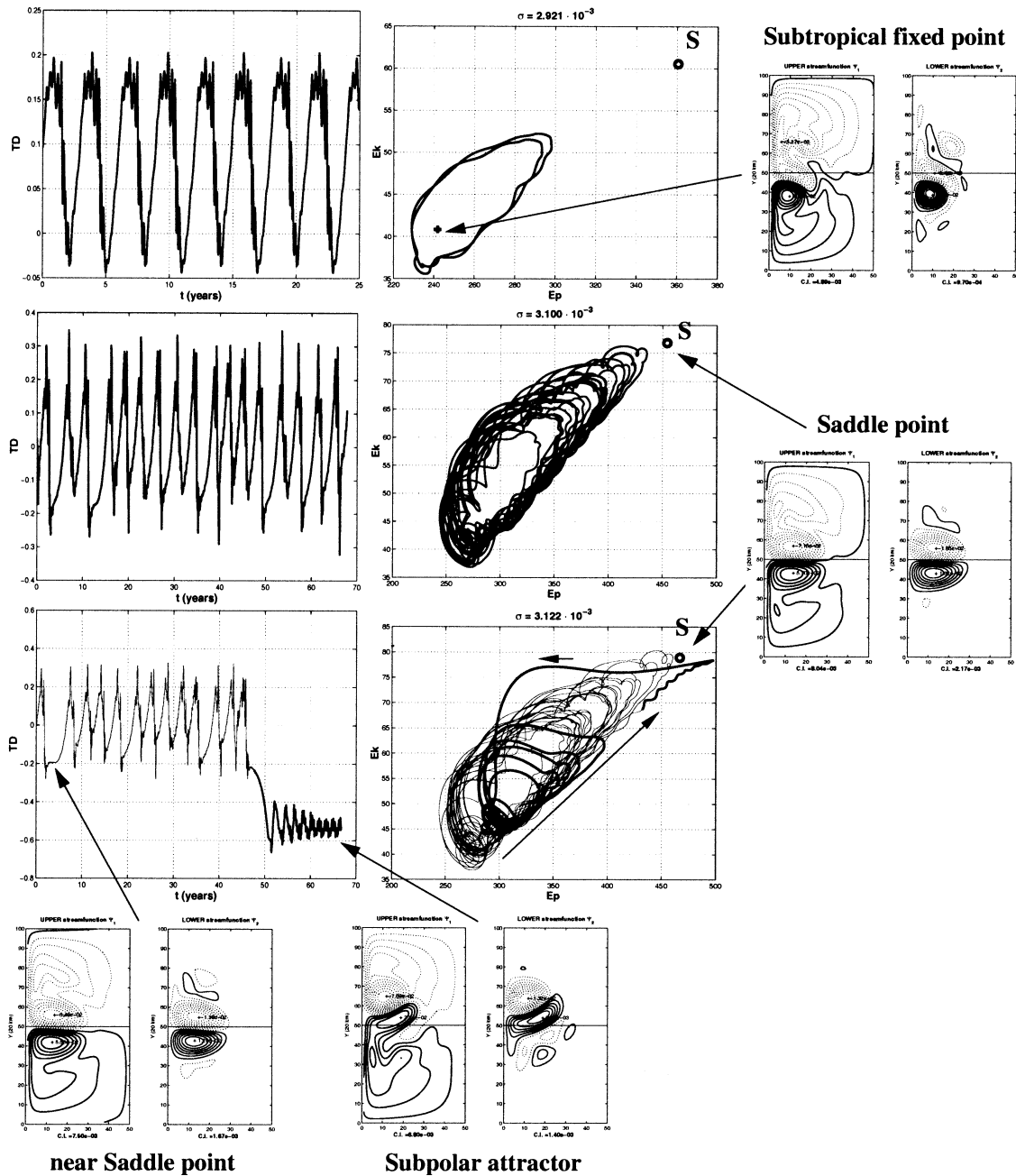


FIG. 5. Behavior of the time-dependent solutions that start near the subtropical branch for  $\sigma = 2.921 \times 10^{-3}$ ,  $\sigma = 3.100 \times 10^{-3}$ , and  $\sigma = 3.122 \times 10^{-3}$ . Time series of TD are shown in the left column and projections of the trajectory onto the  $(E_p, E_k)$  plane in the middle column. Streamfunction patterns are shown in the figure's right and bottom margins; they are referred by arrows to points on the trajectory, among which S refers to the saddle point, i.e., to the unstable steady state on the perturbed-symmetric branch. The streamfunction plots for S are computed at  $\sigma = 3.122 \times 10^{-3}$ ; the ones for the fixed point on the subtropical branch are at  $\sigma = 2.921 \times 10^{-3}$ , while the instantaneous snapshots of the trajectory for the subpolar attractor and near the saddle point (bottom) are also at  $\sigma = 3.122 \times 10^{-3}$ .

with a period of  $4T \approx 10$  yr for  $\sigma = 2.947 \times 10^{-3}$  (see Fig. 4). The dynamics becomes chaotic soon after this value (see also Lin et al. 1989; Legras and Ghil 1983). This presumably infinite cascade of bifurcations occurs before the second Hopf bifurcation detected by the linear stability analysis, at  $\sigma_2^{(ro)} = 2.97 \times 10^{-3}$ . The presence of this cascade prevents the linear modes that be-

come unstable at  $\sigma \geq \sigma_2^{(ro)}$  from affecting substantially the aperiodic solutions.

As  $\sigma$  increases, the time-dependent solutions become more and more energetic and make frequent excursions into the neighborhood of the unstable fixed point on the perturbed-symmetric branch. Figure 5 describes this situation for increasing values of  $\sigma$ . The transport differ-

ence time series  $TD = TD(t)$  is shown in the left column and projections on the  $(E_p, E_k)$  plane in the middle column.

The uppermost panels correspond to  $\sigma = 2.921 \times 10^{-3}$ , that is, just after the first period-doubling bifurcation. The saddle point on the perturbed-symmetric branch is referred to as  $S$ ; its streamfunction pattern and that of the fixed point on the subtropical branch are shown in the right margin of the figure. The limit cycle around the subtropical branch is elongated in the  $(E_p, E_k)$  plane along a straight line that passes through the subtropical fixed point and  $S$ . The solution does approach  $S$  in the full phase space, where it becomes actually more and more symmetric as it reaches its highest energy level. This behavior becomes even more pronounced as  $\sigma$  increases further: in the second row of panels, the solution is chaotic and almost touches the saddle point  $S$ . The TD time series (left column) shows how frequently this occurs: roughly every 15 years or so, the normalized transport difference reaches values between  $-0.2$  and  $-0.3$  at the same time as the solution is most energetic. Such a coincidence of very low TD and very high  $E_k$  and  $E_p$  occurs near  $t = 10$  yr and  $t = 50$  yr, but not for  $t = 40$  yr, for instance.

The third row of panels exhibits, for  $\sigma = 3.122 \times 10^{-3}$ , a transition from the neighborhood of the subtropical branch to that of the subpolar one, with the solution's trajectory eventually converging to a limit cycle surrounding the subpolar branch; a snapshot of the flow pattern along this limit cycle appears at the bottom of the figure's center column. The TD time series at bottom left clearly indicates that, at this value of the wind stress forcing, the solution may spend several years in the vicinity of the unstable fixed point  $S$  (see the pair of panels in the figure's lower-left corner). The  $L_2$  distance between the saddle point on the perturbed-symmetric branch and the time-dependent solution is, in fact, quite small in the full phase space when TD is close to  $-0.2$ , hence the two flow patterns shown at the bottom and in the right margin of Fig. 5 are very similar.

All these pieces of evidence strongly point to a global bifurcation having occurred some where between  $\sigma = 3.100 \times 10^{-3}$  and  $\sigma = 3.122 \times 10^{-3}$ . To consolidate the case further, we compute the unstable manifold of the saddle point for  $\sigma = 2.77 \times 10^{-3}$  and for  $\sigma = 3.11 \times 10^{-3}$ . The unstable real mode that renders the symmetric-branch solutions unstable is multiplied by a small quantity and either added to or subtracted from the steady state. Thus the two directions of the one-dimensional unstable manifold are used as initial directions that point away from the saddle; all the other directions are stable. The flow pattern of the saddle point itself is shown in Fig. 6 in the upper-left corner and that of the unstable linear mode is just below it, in the left margin. This unstable real mode has a flow pattern that is itself symmetric with respect to the line of zero wind stress curl and is responsible for the symmetry-breaking mechanism in the double-gyre circulation (Dijkstra and Kats-

man 1997; Ghil et al. 2002b; Simonnet and Dijkstra 2002). Depending on its sign, it gives the direction of the unstable manifold off the perturbed-symmetric branch toward the subpolar or subtropical branch.

As seen in the upper-central panel of Fig. 6, for  $\sigma = 2.77 \times 10^{-3}$ , the solution converges either to the subpolar or the subtropical branch, depending on the sign of the perturbation; the convergence occurs at slightly different rates since the symmetry is perturbed in the SW equations. The situation is quite different when one conducts the same experiment for  $\sigma = 3.110 \times 10^{-3}$  (lower-central panel in the figure). In the latter case, the solution meanders for a while around the subtropical branch but is eventually attracted by the subpolar branch, independently of the sign of the perturbation. This confirms the result obtained for  $\sigma = 3.122 \times 10^{-3}$  at the bottom of Fig. 5.

Dynamical systems theory suggests that we are in the presence of a so-called homoclinic explosion, in a context where the symmetry is perturbed. The chaotic behavior of the solution before and after this global bifurcation is characteristic of the Shilnikov (1965) phenomenon associated with a homoclinic orbit of saddle-focus type. In such a case, one expects a cascade of period-doubling bifurcations and saddle-node bifurcations in the Poincaré map induced by the basic limit cycle, as well as an infinite number of multiple-pulse homoclinic orbits at and near the bifurcation value (Guckenheimer and Holmes 1990; Wiggins 1987). This theoretical scenario explains the numerically observed period-doubling bifurcation shown in Fig. 4.

The ordering of the eigenvalues at the saddle point on the perturbed-symmetric branch provides information on the type of chaos observed. A linear stability analysis at this point and for  $\sigma$  values near the homoclinic explosion gives two real eigenvalues that are closest to the imaginary axis—the least positive and least negative ones—and two complex conjugate pairs that correspond to symmetric Rossby waves. For the  $\sigma$  interval within which the global bifurcation lies, these eigenvalues are nearly constant, and we list them in decreasing order of their real parts, to wit:  $+0.0387 \pm 0.2995i$ ,  $+0.0317$ ,  $-0.01226$ , and  $-0.0206 \pm 0.0033i$ ; all other eigenvalues have more negative real parts.

The original Shilnikov (1965) scenario involves a homoclinic orbit reconnected to a fixed point of saddle-focus type, with rapid ejection in one (real) direction and slow spiraling in within a tangent plane spanned by two other directions (see also Ghil and Childress 1987). The present situation corresponds to a slight generalization in which the relatively rapid ejection occurs in the unstable 3D manifold whose tangent hyperplane at the saddle focus is spanned by the eigenvectors that correspond to the first three eigenvalues listed above, while the relatively slow spiraling occurs predominantly in the 3D submanifold associated with the remaining three eigenvalues above; finally, the high-dimensional rest of the stable manifold collapses itself rather rapidly

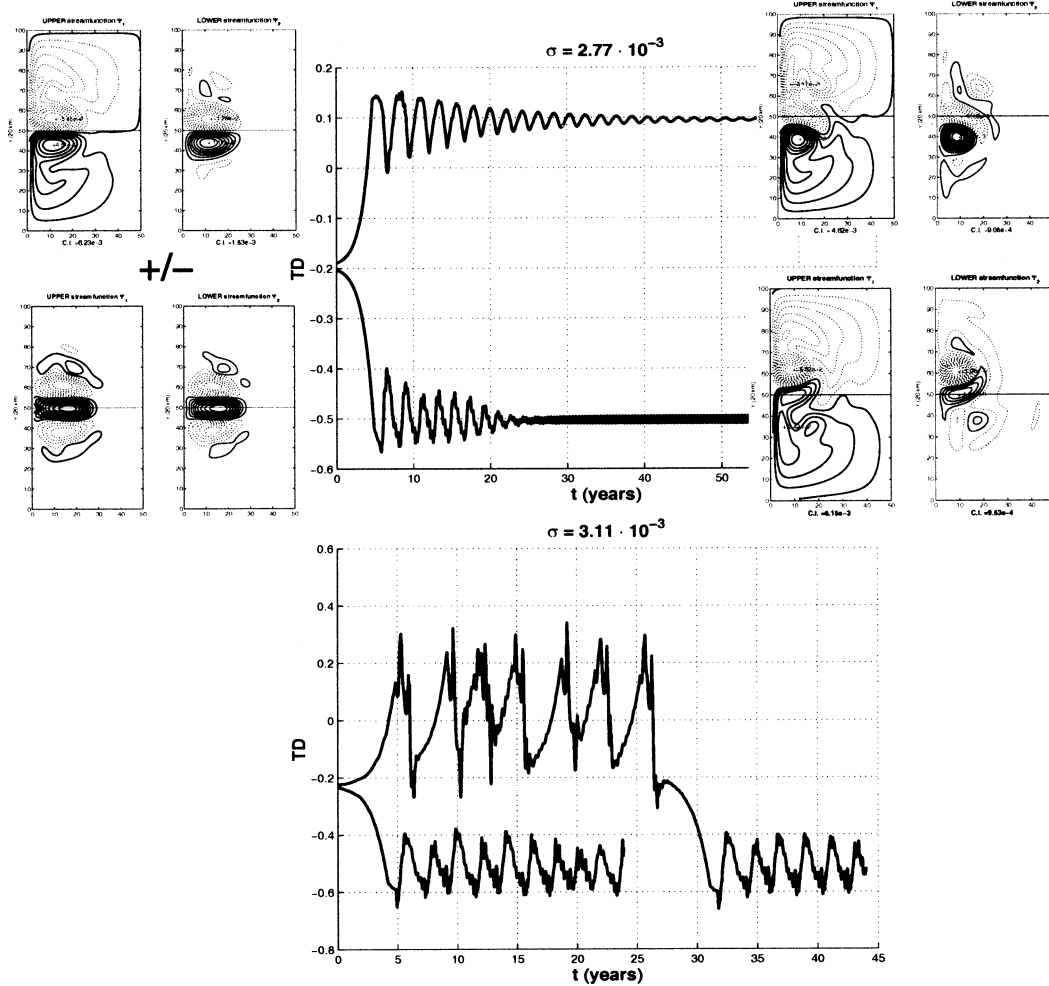


FIG. 6. Transition between branches near the first homoclinic explosion, off the subtropical branch. Central panels: TD time series that start from the initial states shown at left for  $\sigma = 2.77 \times 10^{-3}$  (upper panel) and  $\sigma = 3.11 \times 10^{-3}$  (lower panel). Final states are shown to the right; see text for details.

onto the latter submanifold. The rigorous treatment of such multidimensional cases seems rather limited; see, however, Kuznetsov (1995) for a theorem in  $\mathbb{R}^n$ .

The chaotic behavior just described is robust to changes in the values of other parameters, as indicated by several numerical experiments where the inverse Froude numbers  $F_1$  and  $F_2$ , the Ekman number  $E$ , and the Rossby number  $\epsilon$  were changed, one at a time. Moreover, time integrations on a finer, 10-km grid lead to the same dynamical behavior. This type of transition to aperiodic behavior is not only robust, but also provides an efficient mechanism for generating low-frequency behavior on an interannual scale. Interdecadal variability arises next, when another homoclinic orbit is created off the subpolar branch.

*b. The subpolar-branch attractors*

The subpolar branch of limit cycles, immediately after the first Hopf bifurcation at  $\sigma_1^{(pol)} = 2.717 \times 10^{-3}$ , is

characterized by higher-frequency variability than the subtropical branch. Numerical solutions have a subannual period of  $T_1^{(pol)} = 5$  months that agrees with the linear results shown in the two uppermost panels of Fig. 1. The spatiotemporal behavior of this first oscillatory instability is shown in Fig. 1 as mode 1 (middle row of panels).

The limit cycle that arises from this instability's finite-amplitude saturation is destabilized through a second Hopf bifurcation for  $\sigma \geq \sigma_2^{(pol)} = 2.905 \times 10^{-3}$ . The trajectories are now quasiperiodic and lie on a 2-torus. Figure 7 shows limit cycles, for  $\sigma_1^{(pol)} < \sigma < \sigma_2^{(pol)}$ , and toroidal attractors for  $\sigma > \sigma_2^{(pol)}$ , projected onto the  $(E_p, E_k)$  plane. These 1 and 2 tori are spanned by the finite-amplitude version of the two linear modes labeled 1 and 2 in Fig. 1.

The key role played by these two modes is confirmed by the spectral analysis of potential-energy time series taken from three of the attractors shown in Fig. 7, labeled A, D and G. The results of this analysis reveal

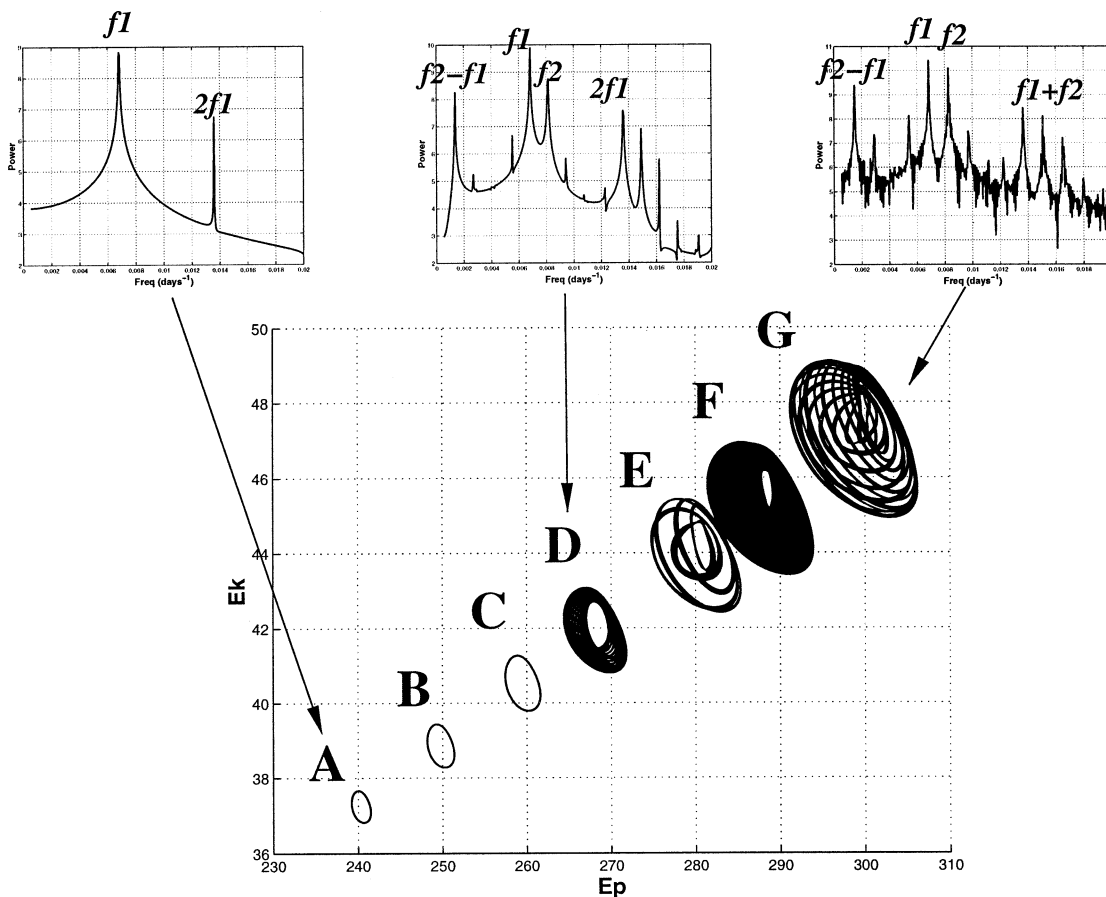


FIG. 7. Limit cycles and toroidal attractors around the subpolar branch for increasing values of  $\sigma$ . Large lower panel: projection of the limit cycles and 2-tori onto the  $(E_p, E_k)$  plane: (A)  $\sigma = 2.800 \times 10^{-3}$ , (B)  $\sigma = 2.850 \times 10^{-3}$ , (C)  $\sigma = 2.900 \times 10^{-3}$ , (D)  $\sigma = 2.942 \times 10^{-3}$ , (E)  $\sigma = 3.000 \times 10^{-3}$ , (F)  $\sigma = 3.035 \times 10^{-3}$ , and (G)  $\sigma = 3.085 \times 10^{-3}$ . The three small upper panels are power spectra of the corresponding  $E_p$  time series for the solutions labeled A, D, and G, using the standard fast Fourier transform algorithm. The frequencies  $f_1 = 1/147 \text{ day}^{-1}$  and  $f_2 = 1/122 \text{ day}^{-1}$  are nearly constant over the range of  $\sigma$  analyzed.

two distinct dominant frequencies,  $f_1 = 6.795 \times 10^{-3}$  ( $f_1 = 147 \text{ day}^{-1}$ ) and  $f_2 = 8.172 \times 10^{-3}$  ( $f_2 = 122 \text{ day}^{-1}$ ), at  $\sigma = 2.942 \times 10^{-3}$ . These two are remarkably close to the frequencies computed by the linear analysis whose results were plotted in Fig. 1:  $T_1^{(\text{pol})} = 148 \text{ days}$  and  $T_2^{(\text{pol})} = 120 \text{ days}$ . It is interesting that the two basic frequencies obtained for the nonlinear, finite-amplitude solutions do not vary as  $\sigma$  increases, although the periods of the two linear modes, 1 and 2, both decrease as  $\sigma$  increases in Fig. 1 (upper-left panel). The 1- and 2-tori obtained for  $2.8 \times 10^{-3} \leq \sigma \leq 3.1 \times 10^{-3}$  fill a relatively small region in phase space (Fig. 7), as the amplitude of their energy variations is small. This could explain why the linear analysis gives such accurate results.

The constancy of these two independent frequencies for a small  $\sigma$  interval suggests the presence of a “Devil’s staircase” (e.g., Jin et al. 1994, 1996; Tziperman et al. 1994, and references therein). Hence, as  $\sigma$  increases, frequency locking is likely to set in. This phenomenon

does seem to occur in Fig. 7 for the tori E and G, which actually appear to be much closer to a periodic solution with a very long period than to a truly quasi-periodic solution that is dense on a 2-torus, like D or F.

When  $\sigma$  approaches the value  $3.20 \times 10^{-3}$ , the 2-torus becomes unstable and the trajectory is attracted toward a larger-amplitude limit cycle of period  $T = 785 \text{ days}$  (not shown). This periodic solution does not live on the torus itself and has a much larger range of energy variation than the previous solutions. Such behavior is somewhat surprising since the appearance of stable limit cycles in this situation arises in general from frequency locking, as in the cases E and G in Fig. 7. Another global bifurcation seems therefore to occur around  $\sigma = 3.20 \times 10^{-3}$ , possibly a collision of one of the previous tori with a limit cycle like the ones shown in Fig. 8.

In fact, all the subtropical trajectories shown in Figs. 5 and 6, when destabilized, converge to a low-frequency, large-amplitude and stable subpolar limit cycle and not to the tori of Fig. 7. This is so even for values of

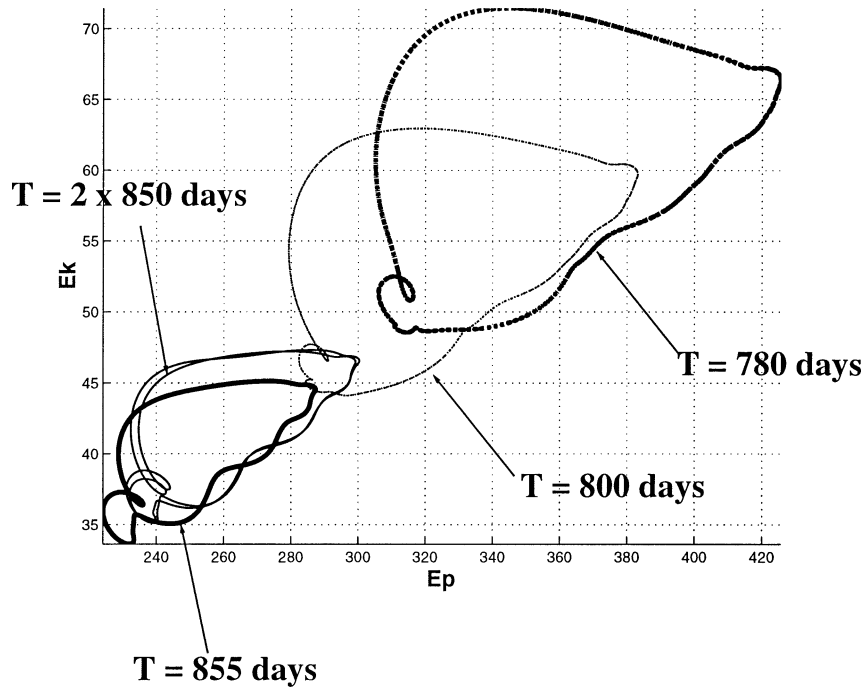


FIG. 8. The  $(E_p, E_k)$  projection of subpolar limit cycles for  $\sigma$  values increasing as  $\sigma = 2.820 \times 10^{-3}$  (heavy solid:  $T = 855$  days);  $\sigma = 2.857 \times 10^{-3}$  (light solid:  $T = 2 \times 850$  days);  $\sigma = 3.104 \times 10^{-3}$  (light dashed:  $T = 800$  days); and  $\sigma = 3.220 \times 10^{-3}$  (heavy dashed:  $T = 780$  days).

$\sigma < 3.20 \times 10^{-3}$ , that is, when these tori are stable. We have therewith an interesting case of coexistence of two stable families of attractors.

We investigate next the family of large-amplitude limit cycles by decreasing smoothly the intensity  $\sigma$  of the wind stress. As  $\sigma$  decreases, so does the amplitude of the limit cycles, although it remains much larger than the amplitude of the tori that coexist with them (cf. Figs. 7 and 8). These limit cycles appear therewith, at first to arise by a supercritical Hopf bifurcation; their period, however increases regularly as  $\sigma$  decreases and reaches 855 days for  $\sigma = 2.820 \times 10^{-3}$ . A period-doubling bifurcation near  $\sigma = 2.857 \times 10^{-3}$  indicates that, actually, more complex bifurcations may occur in this neighborhood. We did not explore these phenomena further since this family of solutions becomes again simply periodic for smaller values of  $\sigma$ . For  $\sigma < 2.820 \times 10^{-3}$ , these limit cycles become unstable and the solution converges to one of the smaller limit cycles around the subpolar branch that are spanned by the subpolar mode 1 in Fig. 1 (between cases A and B in Fig. 7).

The origin of this family of limit cycles remains unexplained. It could arise from another isolated branch of solutions that was not detected in Part I. Newton algorithms using various initial states in the vicinity of the limit cycle's mean state, or other "educated guesses," either converge to the already-known subpolar branch or do not converge at all.

Figure 9 shows the mean state (pair of uppermost

panels) and the streamfunction anomalies (four pairs of lower panels) of one of these limit cycles, at the lowest value of  $\sigma$  at which it is stable, that is, at  $\sigma = 2.820 \times 10^{-3}$ . These limit cycles clearly correspond to oscillatory gyre modes that propagate northwestward (cf. Fig. 9 with Fig. 2). This family should thus be related, through the perturbed mirror symmetry which prevails in the SW models, to the oscillatory gyre modes found around the subtropical branch. Moreover, the amplitude of these subpolar limit cycles in the  $(E_p, E_k)$  plane (not shown) is comparable to those spanned by the subtropical oscillatory gyre mode (see Figs. 4 and 5).

For a slightly more intense wind stress, the large limit cycles of Fig. 8 become unstable between  $3.225 \times 10^{-3} < \sigma < 3.233 \times 10^{-3}$ . Time series analysis reveals chaotic behavior at  $\sigma = 3.245 \times 10^{-3}$ . This transition to chaos occurs within a very narrow  $\sigma$  interval and the details do not seem to affect subsequent behavior at larger  $\sigma$ . Fourier analysis, prefiltered or not, yields two spectral peaks: a dominant one around 710 days, coming from the original period  $T_{3}^{(pol)}$ , and a weaker one at 350 days (not shown). Note that, at this value of  $\sigma$ , the oscillatory gyre mode 3 off the subpolar branch has already become unstable (see Fig. 1); its associated period of  $T_{3}^{(pol)} = 290$  days, however, does not seem to appear in the spectrum of the time series. This reinforces the impression that the chaotic dynamics does not arise from the competition of oscillatory instabilities off the

$\Psi$

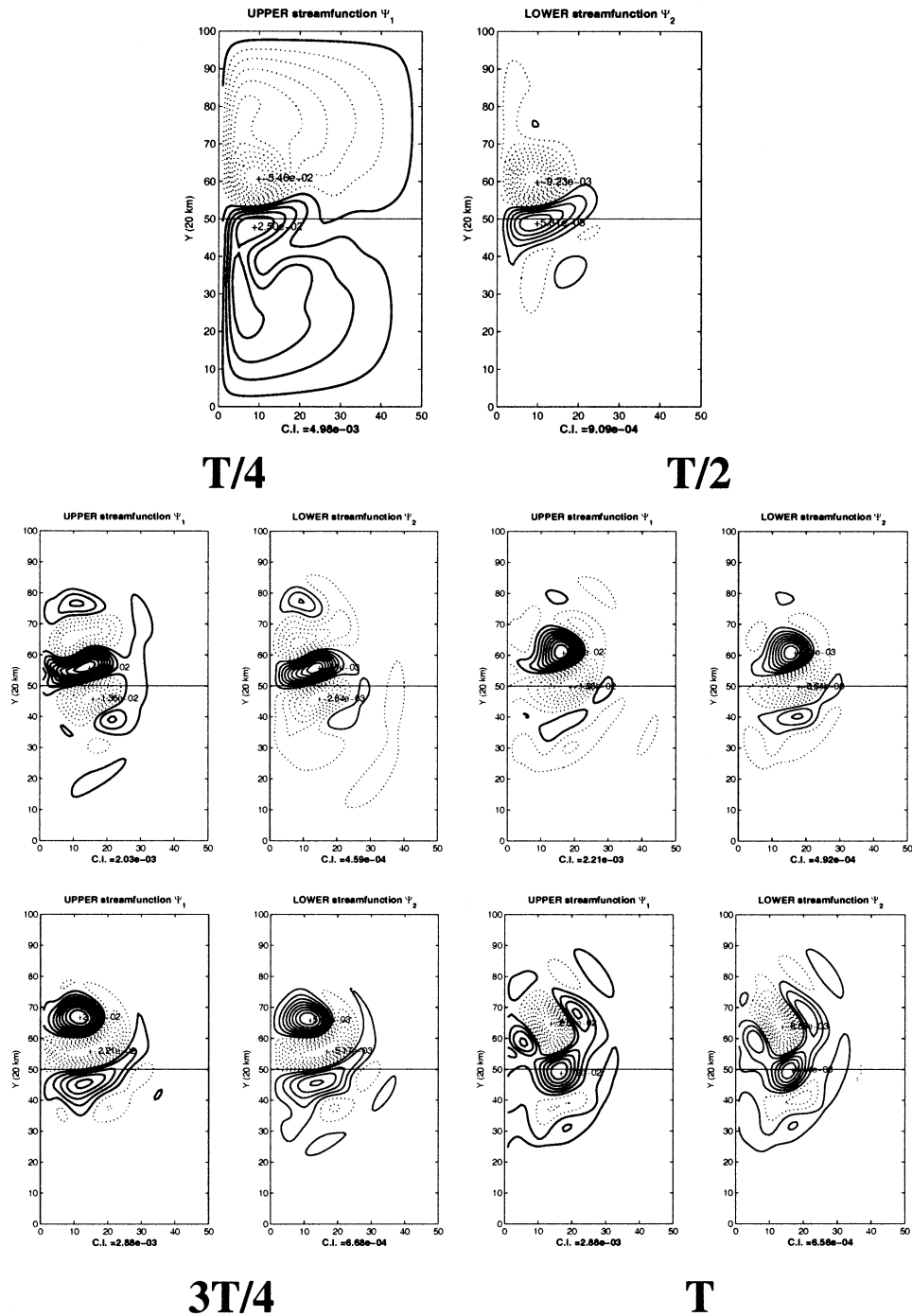


FIG. 9. Mean state (pair of uppermost panels) and streamfunction anomalies of the smallest limit cycle shown in Fig. 8, i.e., for  $\sigma = 2.820 \times 10^{-3}$  and  $T = 855$  days; the anomalies are shown for every quarter period (pairs of panels labeled  $T/4$ ,  $T/2$ ,  $3T/4$ , and  $T$ ).

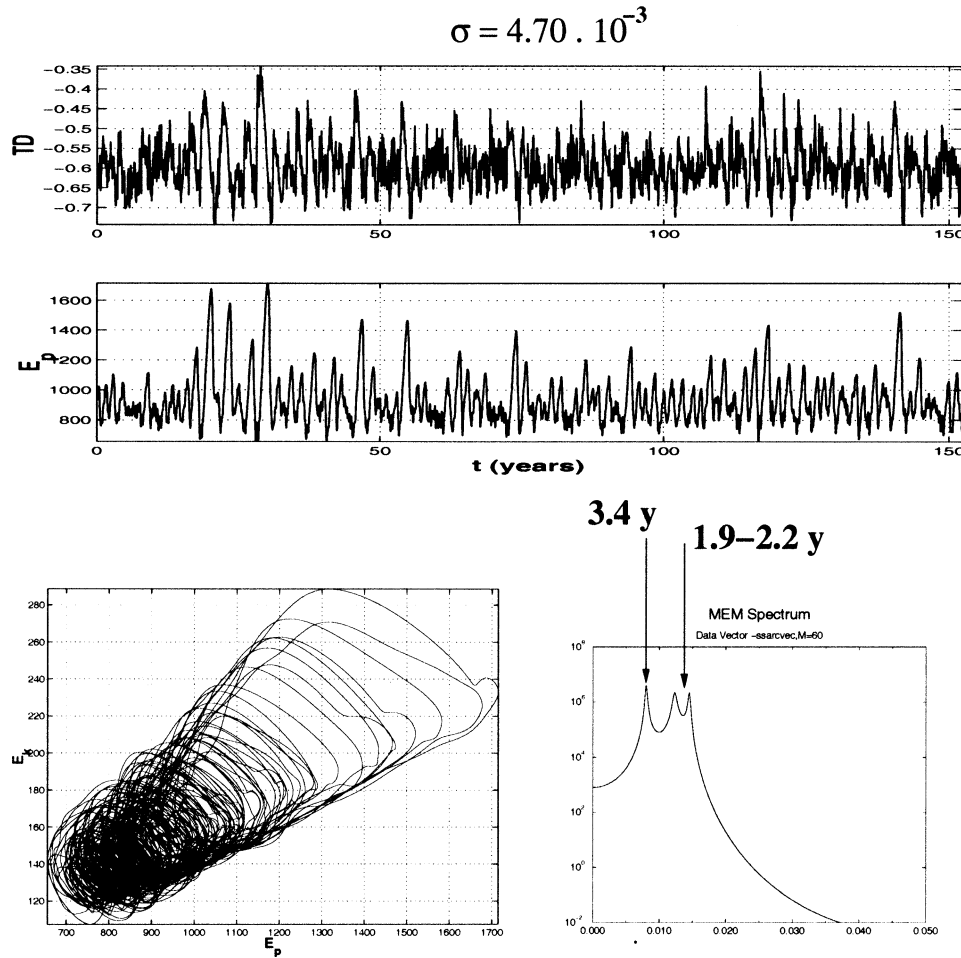


FIG. 10. Chaotic subpolar solution for  $\sigma = 4.70 \times 10^{-3}$ . The upper two panels give the time series of TD and  $E_p$ , while the lower-left panel displays the projection onto the  $(E_p, E_s)$  plane. The lower-right panel gives the maximum entropy spectrum of the potential energy time series after SSA prefiltering; the order of the MEM is = 60, SSA window width = 16 yr, and the number of reconstructed components = 8 (see Dettinger et al. 1995; Ghil et al. 2002a).

subpolar branch itself but from global effects in phase space.

In Fig. 10, the situation for a much larger value of  $\sigma = 4.70 \times 10^{-3}$  is presented. The solution is much more irregular than in Figs. 5–8 (see the two upper panels). Still, the spectrum of the potential energy (lower-right panel) has peaks that are very similar to those before, that is, at  $\sigma = 3.245 \times 10^{-3}$ , with robust signatures around 2 and 3 years but none around 1 year. To suppress the broadband noise a prefilter based on singular-spectrum analysis (SSA: see Dettinger et al. 1995; Ghil et al. 2002a; and Part I of this study) has been applied in Fig. 10. Note that, as one reduces the SSA window width to 2 years or so (not shown), the 140-day peak related to Rossby wave propagation (mode 1) also emerges distinctly; its 120-day companion (mode 2) is present as well, but to a lesser extent.

In this regime, the orbits stay in the vicinity of the subpolar branch, being characterized by entirely nega-

tive TD values. Very energetic oscillations of relaxation type are associated with the high-energy spikes seen in the time series of the potential energy (Fig. 10, second panel from the top). The spatiotemporal behavior of the flow (not shown) corresponds to a high-amplitude version of the subpolar oscillatory gyre modes shown in Fig. 9. The relaxation phase of these oscillations, when the energy drops suddenly, is dominated by both eddy formation and the Rossby wave dynamics responsible for the 4–5 month variability.

In the next section, a typical relaxation oscillation, similar to the ones in Fig. 10, is described. We also show that, in some parameter regimes, transitions from the subpolar to the subtropical branch occur as well.

### c. Perturbed homoclinic orbits

We performed a set of experiments with a wind stress forcing of  $\sigma = 4.00 \times 10^{-3}$  and different values of the

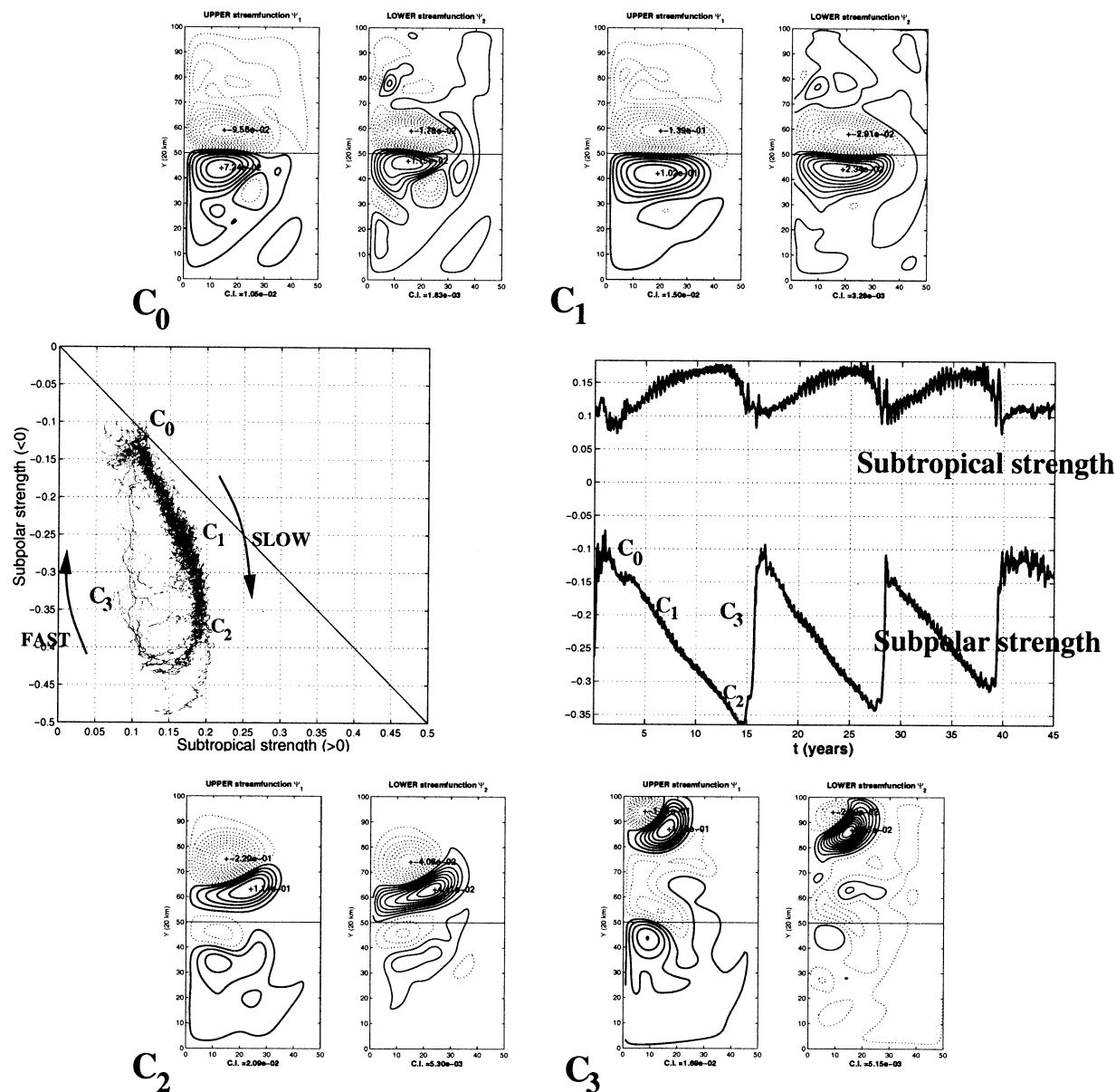


FIG. 11. Approximate homoclinic orbit for  $\sigma = 4.00 \times 10^{-3}$ ,  $A = 200 \text{ m}^2 \text{ s}^{-1}$  and  $\epsilon = 0.033$ . The large panel at center right shows the time evolution of the strength  $h_{i,\text{MAX}} - 1$  of the subtropical gyre (positive) and the strength  $h_{i,\text{MIN}} - 1$  of the subpolar gyre (negative); see Eq. (24) in Part I. The large center-left panel is a projection of the orbit onto the plane spanned by the strength of the subpolar vs the subtropical gyre. Streamfunction flow patterns are shown for the four phases  $C_0$ ,  $C_1$ ,  $C_2$ ,  $C_3$  of the recirculation dipole's life cycle in pairs of small panels at the top ( $C_0$  and  $C_1$ ) and bottom ( $C_2$  and  $C_3$ ) of the figure. The arrows in the center-left panel identify the sense and rate of the evolution around the orbit.

Rossby number  $\epsilon$  [see discussion that follows Eqs. (4) and (5) in Part I]. For these experiments, we used a viscosity of  $A = 200 \text{ m}^2 \text{ s}^{-1}$  that is smaller than the viscosity of  $A = 300 \text{ m}^2 \text{ s}^{-1}$  used so far.

Homoclinic orbits are structurally unstable and thus cannot be obtained exactly by standard methods of computing forward trajectories in high-dimensional dynamical systems like our  $2\frac{1}{2}$ -layer SW model. Their presence is, however, manifest in the characteristics of nearby orbits in phase space. Moreover, the proximity of a

homoclinic bifurcation of codimension 1 in parameter space tends to organize the chaotic flow dynamics in a very specific way. Two different cases of such behavior are described in the following.

The value of  $\epsilon = 0.033$  taken here is higher than the value 0.02 used so far (see Table 1). The system's dynamical behavior is dominated by the life cycle of a strong, nearly antisymmetric dipole structure (see uppermost and lowermost panels in Fig. 11). The two large central panels of Fig. 11 show the time evolution of this

life cycle in terms of the strengths of the subtropical and the subpolar gyre [maximum and minimum of the thickness anomalies of the upper layer, respectively; see figure caption here and Eq. (24) in Part I]. The sawtooth shape apparent in particular in the subpolar gyre's strength (center-right panel) indicates a relaxation oscillation. The oscillation's extreme phases, as well as its slow-growth and rapid-decay phases, are identified in the figure by the symbols  $C_0$ – $C_3$  and by the arrows in the phase-plane projection at center-left.

In phase  $C_0$ , two vortices of minimal and nearly equal strength, as well as relatively small and nearly equal size, occupy the recirculation zone. In phase  $C_1$ , both cells of opposite vorticity grow slowly in size as well as intensity until they nearly reach the eastern wall of the basin. In phase  $C_2$ , the cyclonic, subpolar cell is considerably stronger than the anticyclonic, subtropical one. This breaks the symmetry of the quasi-stable dipolar structure, which tilts suddenly away from the axis of symmetry and drifts rapidly northwestward. In phase  $C_3$ , the vorticity in the recirculation zone has nearly disappeared, while a small dipole survives in the basin's northwestern corner. At this point, the slow-growth phase is ready to start all over again.

The phase-plane projection of the trajectory (center-left panel in Fig. 11) is suggestive of the existence of an exact homoclinic orbit at a nearby point in parameter space. The slow and energetic part of the evolution corresponds in general to the fixed point's stable manifold and the fast part to the unstable one. However, in this case, the homoclinic bifurcation has already occurred for a smaller value of  $\sigma$  so that the orbit in Fig. 11 misses its exact reconnection with the fixed point of saddle-focus type. The perturbed-symmetric branch of solutions indeed exhibits flows very similar in pattern to the instantaneous snapshot  $C_1$ : this confirms the role played by an earlier homoclinic bifurcation, such as the one described in section 3a and for a different parameter regime, off this branch.

The mean oscillation period of this dipole's life cycle is  $\sim 13$  yr over the 170-yr time series analyzed. Smaller-amplitude, more irregular fluctuations are superimposed on it and have a monthly timescale. These irregular fluctuations seem to be associated with the homoclinic tangle that arises due to the plotted trajectory's missing exact reconnection. A similar coexistence of rapid, irregular oscillations with slower and more regular ones has also been documented in QG models (Primeau 1998; Berloff and McWilliams 1999; Meacham 2000; Ghil et al. 2002b).

We next decrease the value of the Rossby number to  $\epsilon = 0.025$ . The two time series in Fig. 12 show positive and negative TD values that alternate, as do low and high  $E_p$  values. In the figure's uppermost pair of panels, we plot the mean composite of the solution when  $TD > 0$ ; four of the years used in the compositing are circled here. It is clear that, in this phase A, the solution dwells near the subtropical branch of steady states. Phase A is

thus referred to as subtropical, in contrast with the subpolar one shown in the lower-right panel of Fig. 12 (labeled C). The streamfunction of the latter is also obtained by performing a composite analysis with the constraint that  $TD < -0.3$  and  $E_p < 700$  simultaneously, that is when the solution has low energy and a more intense subpolar recirculation.

The dipole's life cycle resembles somewhat the one exhibited in Fig. 11. In particular, one observes a similarly slow growth phase of a nearly antisymmetric dipole labeled B in Fig. 12 (lower-left pair of panels); its flow pattern corresponds more or less to the state referred to as  $C_1$  in Fig. 11. However, contrary to the previous case, the dynamics is characterized by the appearance of two distinct flow regimes: they correspond either to solutions in the vicinity of the subtropical branch, phase A, or to solutions in the vicinity of the subpolar branch, phase C. These two types of solution behavior occur both during the generation of the smaller eddies, that is, just after the high-energy dipole B, with its extended and straight eastward jet, has collapsed. Spectral analysis of the time series exhibits a pronounced peak around 7 yr (not shown), which equals the mean period of the dipole's life cycle. Interdecadal variability is also generated by the irregular transitions between regimes.

The chains of regime transitions  $A \rightarrow B \rightarrow A$ ,  $C \rightarrow B \rightarrow C$ ,  $A \rightarrow B \rightarrow C$  or  $C \rightarrow B \rightarrow A$  are most frequent. We have not observed direct transitions between regimes A and C, without the appearance of the slow-growth phase B.

The solutions that leave the vicinity of the weakly unstable subtropical branch in section 3a follow the same spatiotemporal sequence: a strong, antisymmetric dipolar structure grows in size and in intensity until it is destabilized and gives birth to new dynamics in the vicinity of the subpolar branch. This transition corresponds to the previous path  $A \rightarrow B \rightarrow C$ , except that C in this case is a stable periodic solution off the subpolar branch (one of the limit cycles of Fig. 8).

We suspect that the transitions between a subtropical and a subpolar flow regime also have their roots in an earlier homoclinic bifurcation. Chang et al. (2001) observed trajectories in phase space that span both attractors, subpolar and subtropical. In a QG model with exact symmetry, it is expected that the homoclinic explosion associated in the present study with the isolated branch occurs simultaneously—that is, at the same parameter value—on both the subpolar and subtropical branch. A symmetric homoclinic orbit can thus organize the whole dynamics of the barotropic double-gyre circulation as the nonlinearity is increased. Nadiga and Luce (2001) have recently documented this phenomenon in a barotropic, reduced-gravity QG model.

For particular parameter settings, these symmetric homoclinic orbits may survive the natural lack of symmetry of the SW equations; alternatively, a second, subpolar homoclinic bifurcation occurs after the subtropical

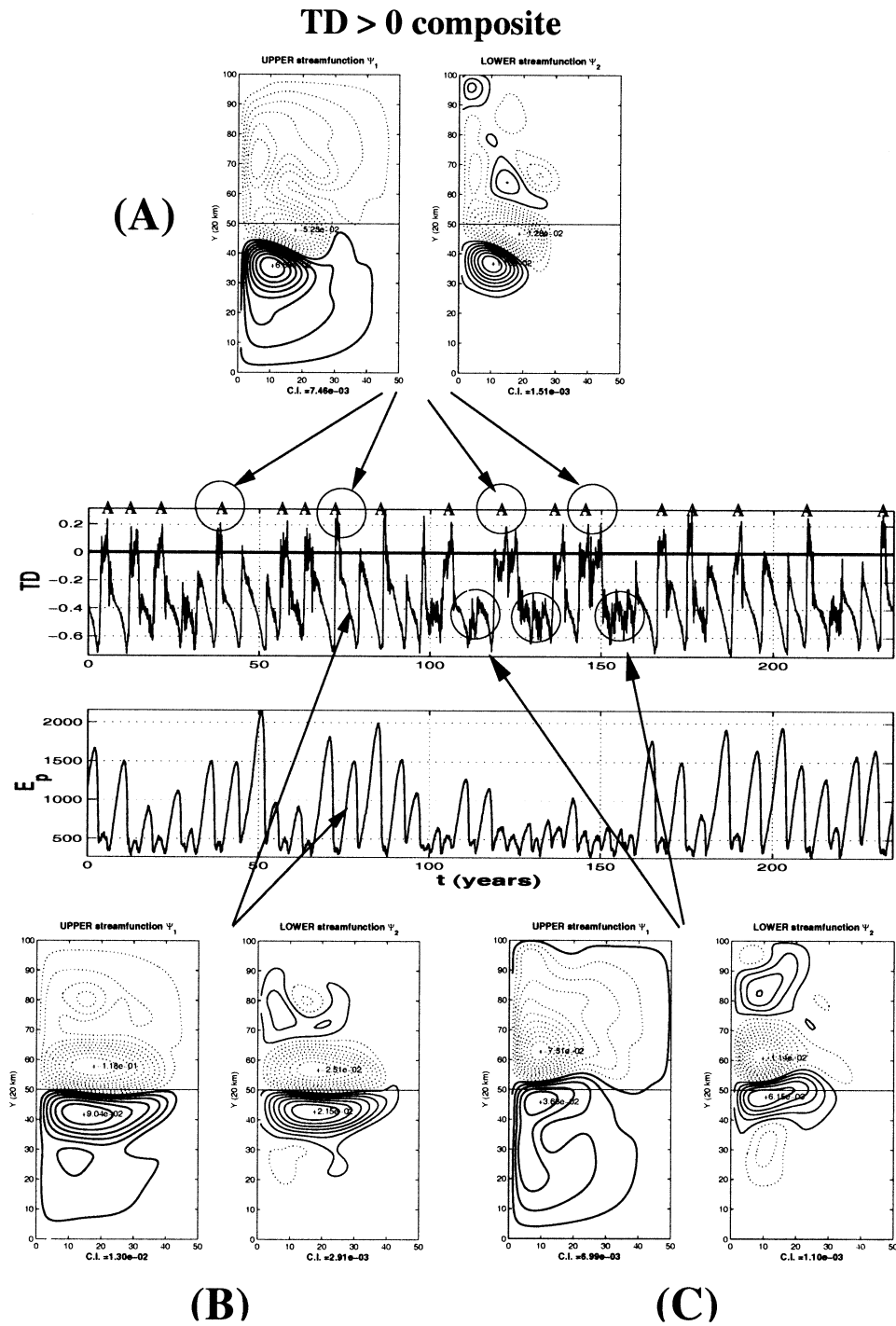


FIG. 12. Approximate homoclinic orbit that spans all three branches, for  $\sigma = 4.00 \times 10^{-3}$ ,  $A = 200 \text{ m}^2 \text{ s}^{-1}$ , and  $\epsilon = 0.025$ . The two large central panels show the time series of TD (upper) and  $E_p$  (lower). Flow patterns are shown in the pairs of smaller panels above and below, for the three preferred regimes: (a) subtropical regime, (b) perturbed-symmetric regime, and (c) subpolar regime. The uppermost pair of panels corresponds to the streamfunction composite (a) of the flow when  $TD > 0$ . The lower pairs of panels corresponds to an instantaneous snapshot of the perturbed-symmetric solution (b) and a composite for the subpolar solutions (c).

homoclinic bifurcation. Thus, due to the lack of symmetry, the simultaneous explosion on both asymmetric branches is delayed: a subtropical homoclinic bifurcation occurs first, as described in section 3a, followed eventually by a subpolar homoclinic bifurcation. Transitions between the two (asymmetric) branches then become possible, although one of the branches may be preferred (see also the sketch of the dynamics in Fig. 16 below).

The first, subtropical homoclinic bifurcation enables transitions  $A \rightarrow B \rightarrow C$ , while the second, subpolar one enables transitions  $C \rightarrow B \rightarrow A$  (see again Fig. 12). In the cases studied here, the fact that the trajectories visit the neighborhood of the perturbed-symmetric branch through the emergence of a symmetric dipole with an extended jet, like in flow pattern  $C_1$  of Fig. 11 and pattern B of Fig. 12, is an indication that such a subpolar homoclinic bifurcation is very likely. We have good visual evidence, based on comparing instantaneous flow patterns (not shown) with those of subtropical steady states, that such a bifurcation occurs in the range  $3.400 \times 10^{-3} < \sigma < 3.450 \times 10^{-3}$ .

Reducing the eddy diffusivity  $A$  seems to be an efficient mechanism for increasing the frequency of regime transitions (not shown). Similarly, for small values of the Rossby number  $\epsilon$ , the dynamics of the SW equations converges to QG dynamics and regime transitions between subpolar and subtropical flows occur more frequently (not shown either).

#### 4. Comparison with observations

##### a. Large rectangular basin

To compare our numerical results with the observed circulation of an ocean basin, we performed two additional sets of numerical simulations that used more realistic geometries. The first followed Speich et al. (1995) in using a rectangular basin close in size to the North Atlantic, that is,  $6400 \text{ km} \times 4400 \text{ km}$ . We applied to it the same idealized zonal wind stress forcing given by Eq. (2) in Part I. The number of unknowns is  $10^6$  when using a horizontal resolution of  $\Delta x = \Delta y = 12 \text{ km}$ . We applied therefore a domain decomposition algorithm with 32 processors on an SGI computer with 128 processors (Scaamp System, Indiana University).

The forcing parameter was chosen to be  $\sigma = 0.20 \times 10^{-1}$ . All other parameters have the same values as in Table 1, except for the horizontal eddy diffusion coefficient, which is now  $A = 150 \text{ m}^2 \text{ s}^{-1}$ . This yields an Ekman number of  $E = 3 \times 10^{-6}$  here versus  $E = 6 \times 10^{-6}$  in Table 1. In all the simulations reported in this section, we started from a solution at rest and eliminated transient behavior by ignoring the first 30–40 years of the time integration. This left in each case a 100-yr-long record for analysis that allows us to capture signal regularities with periods up to a decade or so.

The energy of the system varies irregularly, although

the trajectory is trapped in a small region of the  $(E_k, E_p)$  phase plane (not shown). In order to obtain further information on the model's behavior, we extracted a few principal modes of variability from the time series of global scalar quantities. SSA was applied to the kinetic energy record using a window width of 140 months, as suggested by Moron et al.'s (1998) analysis of observed sea-surface temperatures for the North Atlantic. The power spectrum of the record projected onto the sum of its 12 leading reconstructed components is shown in Fig. 13a.

Three peaks are in evidence in the figure, at 7 years, 2.9 years, and 24 months. To test the robustness of our spectral results, we varied the window width in the SSA algorithm, the number of leading modes used in the prefiltering, and the maximum entropy method (MEM) order in the spectral analysis itself. We also performed the same analysis for different physical quantities, such as potential energy and normalized transport difference TD. All these analyses exhibited the same spectral peaks as seen in Fig. 13a.

The flow patterns in the two panels of Fig. 13b show a fairly smooth Sverdrup interior in the eastern part of the basin. Complex interactions among multiple vortices occur in the recirculation zone, near the detachment of the eastward jet from the western boundary, like in the smaller,  $1000 \text{ km} \times 2000 \text{ km}$  basin (see Figs. 1–3, 11, and 12). Along the northern boundary, Rossby waves propagate westward with a period of roughly 7–8 months, although this mode of variability does not appear in the SSA analysis of global scalar time series.

We performed different simulations, changing lateral viscosity to  $A = 200 \text{ m}^2 \text{ s}^{-1}$  and  $A = 300 \text{ m}^2 \text{ s}^{-1}$ , and grid resolution to 10 and 20 km. All these simulations exhibit roughly similar results, with at least one robust peak of variability around 6–7 years and two peaks with higher frequency around 3 years and 20–25 months. This is in fairly close agreement with the results of Speich et al.'s (1995)  $1\frac{1}{2}$ -layer model. These authors used a viscosity of  $A = 300 \text{ m}^2 \text{ s}^{-1}$  and a resolution of  $\Delta x = \Delta y = 20 \text{ km}$  throughout their work.

Speich et al. (1995) analyzed the Cooperative Ocean–Atmosphere Data Set (COADS) sea surface temperatures to determine the meridional position of the Gulf Stream and the Kuroshio Extension axis at a fixed longitude. Their spectral analysis of the time series so obtained showed similar peaks: 6 years and 20 months for the Gulf Stream, and 9 years and 29 months for the Kuroshio Extension. As was pointed out by these authors (see also Jiang et al. 1995), the size of the basin is an important factor in the variability: the model's oscillation periods increase with the width of the basin; the periods also seem, in our experiments, to increase slightly with decreased viscosity (not shown). The period of 7–8 months, associated in this version of our SW model with internal Rossby waves, has also been observed in Gulf Stream variability derived from satellite data by Lee and Cornillon (1995).

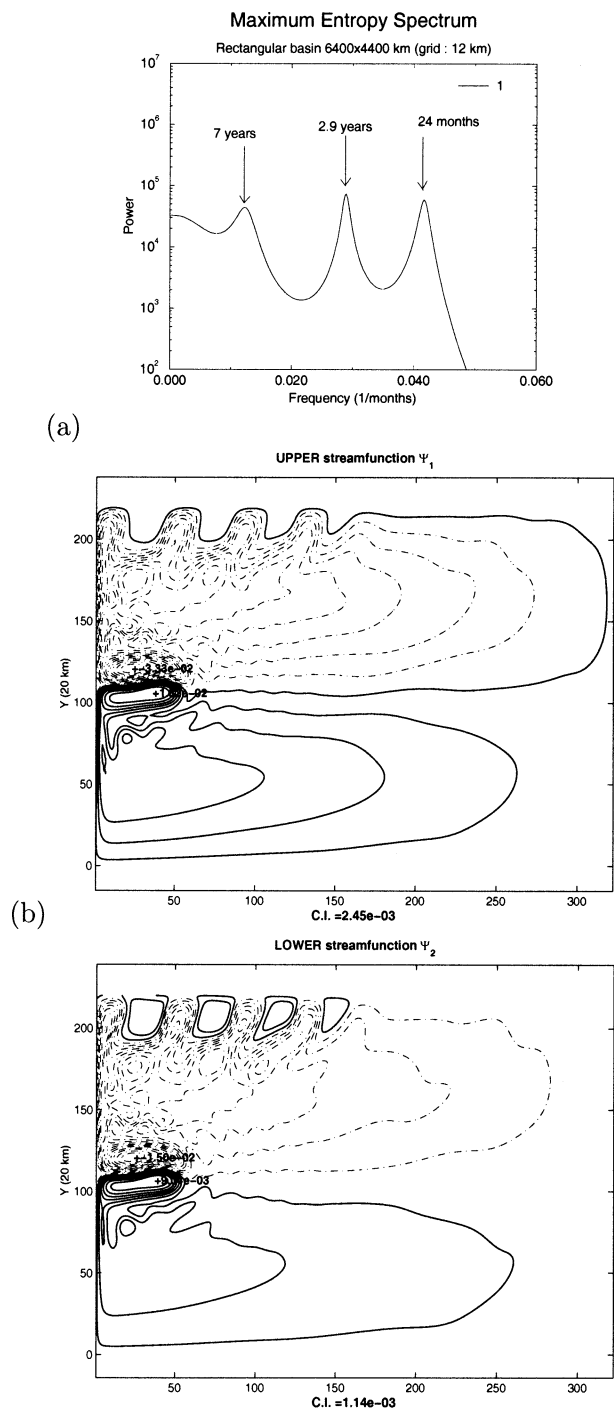


FIG. 13. Model results for a large rectangular basin of  $6400 \times 4400 \text{ km}^2$ . (a) Maximum-entropy spectrum of the SSA-prefiltered kinetic energy time series; the MEM order is 20. (b) Snapshot of the upper- and lower-layer streamfunction at  $T = 100 \text{ yr}$ .

## b. North Atlantic-shaped basin

### 1) IDEALIZED WIND STRESS

We finally performed another simulation in which we approximated the size and shape of the North Atlantic

basin (NAB) using bathymetry data from the DAMEE-NAB database DTM-5, which is updated from ETOPO-5 (see Chassignet et al. 2000). The contour level chosen to define the lateral boundaries for both active layers was at depth 500 m between  $20^\circ$  and  $60^\circ\text{N}$  (see Fig. 14a). The ETOPO-5 geometry was only used to determine the position of the coastlines: the model still has an infinitely deep lower layer and hence no effects of bathymetry inside the basin are included (see Fig. 1 in Part I).

The experiment was performed with an eddy-resolving grid of  $\Delta x = \Delta y = 12 \text{ km}$ , while the eddy viscosity chosen was  $A = 200 \text{ m}^2 \text{ s}^{-1}$ . This equals the value used by Dijkstra and Molemaker (1999) for a North Atlantic-shaped basin with a resolution of roughly 50 km, while Berloff and McWilliams (1999) used  $A$  values from 400 to  $1600 \text{ m}^2 \text{ s}^{-1}$  and resolutions from 15 to 30 km on a square basin of  $3840 \text{ km}$  on each side.

We also took  $H_1 = H_2 = 250 \text{ m}$  and  $U = 0.1 \text{ m}$ , while all the other parameters had the same values as before. This simulation still used the idealized wind stress forcing of Eq. (2) in Part I, with  $D$  now corresponding to  $40^\circ$  of latitude.

We analyzed several scalar time series from the 100-yr record obtained from this simulation after discarding the initial transients. The time series analyzed included the total kinetic and potential energy, the kinetic energy in the subpolar and subtropical gyres, and the (positive and negative) extrema of the upper-layer thickness. We used an SSA prefilter and computed the maximum entropy spectrum of the prefiltered records; the number of reconstructed components retained was 12. We chose different SSA window widths, namely 20 and 5 years, for interannual and subannual variability, respectively. Figure 14b shows the maximum entropy spectrum of the subpolar kinetic energy (light dotted) and the total potential energy (heavy solid). They are representative of the different modes of variability present in the other time series analyzed but not shown here.

One subannual peak of 188 days (6.2 months) is present in all global quantities, such as total kinetic and potential energy. This peak is associated with variations in the subtropical recirculation cell's shape, size, and intensity, as manifested in particular in the maximum of the upper-layer thickness. This maximum is located in the subtropical recirculation cell east of Florida and south of the Gulf Stream, near  $30^\circ\text{N}$ ,  $75^\circ\text{W}$ . The subtropical potential energy also exhibits a 125-day mode (not shown).

The main subannual period of this simulation is thus quite close, in period and characteristics, with the subpolar-branch oscillatory instability of the small, rectangular-basin model of sections 2 and 3 here. As mentioned already, these spatiotemporal characteristics also agree with the main subannual mode of Chang et al.'s (2001) QG barotropic model. The 6-month period agrees furthermore with that found in a 20-yr integration of the Modular Ocean Model (MOM) at  $0.5^\circ$  resolution (A.

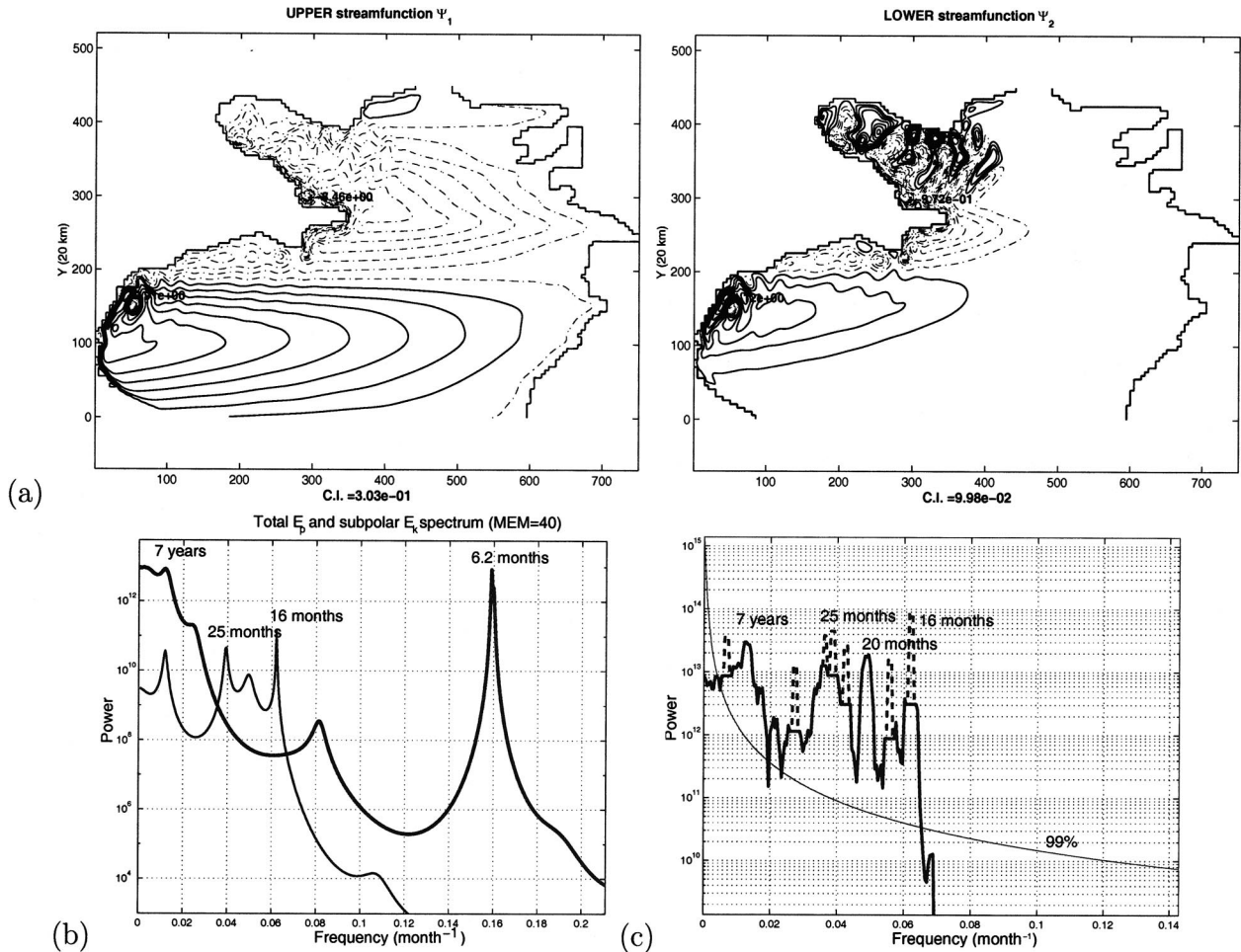


FIG. 14. Model results for a basin that approximates the North Atlantic in size and shape, using an idealized wind stress. (a) Snapshot of the upper- and lower-layer streamfunctions at  $T_0 = 100$  yr; (b) maximum entropy spectrum of the potential energy of the whole basin (heavy solid line) and subpolar kinetic energy (light dotted line). The SSA window width is 20 years, the number of reconstructed components retained = 12, and the MEM order = 40. (c) Multitaper spectrum of subpolar kinetic energy, showing separate spectral components and significance levels: reshaped spectrum (heavy solid line), harmonic spectrum (heavy dotted), and red-noise comparison spectrum (99% confidence level, light solid); see Mann and Lees (1996) and Ghil et al. (2002a) for details.

Wirth, K. Ide, and M. Ghil 1999, personal communication; see also Chassignet et al. 2000).

The subpolar gyre shows vigorous activity characterized by internal Rossby waves that propagate northward into the basin's Labrador Sea. Their period seems to vary between 16 and 25 months. Three separate peaks are apparent in the gyre's kinetic energy at 16, 20, and 25 months (see Fig. 14b) and all three are quite robust. They are also present in the time series of upper- and lower-layer thickness for particular grid points located in this region (not shown). Multitaper spectral estimates performed for the subpolar  $E_k$  using the SSA-Multitaper Method (MTM) Toolkit (Dettinger et al. 1995; Ghil et al. 2002a) give the same three peaks as being significant above the 99% confidence level (Fig. 14c).

An interannual 7-yr mode is clearly apparent in the subpolar kinetic energy (see both Figs. 14b and 14c).

It is not present in quantities characterizing the dynamics of the subtropical gyre. Moron et al. (1998) found a 7–8-yr mode to act on the North Atlantic's whole double-gyre circulation over the last century of sea surface temperature data, while Plaut et al. (1995) identified it also in three centuries of central England temperatures. Moreover, Simonnet (2001) observed a 7.5-yr peak in a 120-yr-long dataset of sea level pressures over the North Atlantic. The spatiotemporal characteristics of this observed oscillation are therewith closer to the 6-yr mode obtained in the large rectangular basin of section 4a here, as well as by Speich et al. (1995), than to the 7-yr oscillation that arises in the present simulation with a more realistic domain shape and still idealized wind stress.

A preliminary experiment that used slightly different numerical parameters and resolution, and a basin that was somewhat less realistic boundaries, was also per-

formed in preparation for the one described above. It yielded, in fact, quite similar results, to wit, a 7-yr subpolar mode together with higher-frequency modes of 6–10 months that arise in the subtropical gyre.

## 2) REALISTIC WIND STRESS

The snapshots of the upper- and lower-layer streamfunction shown in Fig. 14a exhibit a subtropical gyre that is both stronger and occupies a larger area than the subpolar one. This simulation's subpolar gyre is, however, still too large and strong, while the subtropical gyre is still unrealistically regular and smooth. Dijkstra and Molemaker (1999) carried out sensitivity experiments concerning the wind stress field's impact on the circulation for a realistically shaped domain. They used a continuous deformation of the wind stress field—from a purely zonal wind with a sinusoidal profile to a more realistic, climatological vector field of wind stresses due to Hellerman and Rosenstein (1983, HR hereafter). Much more realistic flows were obtained by these authors when using HR wind stress data. In particular, the subpolar gyre had a more realistic size and strength.

We thus performed a simulation using HR wind stresses. Their dataset consists of vector values on a  $2^\circ \times 2^\circ$  grid, which we interpolated to fit our finer Arakawa C grid. We show in Fig. 15 the final snapshot from a simulation that uses a 20-km grid with the same parameters as before, except for  $H_1 = H_2 = 200$  m. For these parameters, the model's Gulf Stream separates slightly north of Cape Hatteras and exhibits meanders that are fairly realistic in position and wavelength, although their amplitude is exaggerated. The size and strength of the subpolar gyre is much more realistic, with the model's North Atlantic Drift now reaching the British Isles. The Gulf Stream shows a tendency to overshoot in other model experiments (not shown) that use larger values of  $H_1$  and  $H_2$ .

We also analyzed spectrally time series taken from the last 90 years of the 120-yr simulation whose final snapshot is shown in Fig. 15. The power spectrum of the total potential energy has three significant spectral peaks, at 6.5 and 7.2 months and at 3.5 years (not shown). The subannual modes are also present in the kinetic energy time series together with some of their harmonics. No signature of a 7-yr oscillation is apparent, though, in this run.

## 5. Concluding remarks

A summary of the results of Part I was given there and will not be repeated here. A key result was the robustness of the perturbed-pitchfork bifurcation that leads to multiple equilibria in the double-gyre circulation. We call the three branches of the “pitchfork” subpolar, perturbed symmetric, and subtropical. The subpolar branch is continuously connected to the limit of no forcing, while the subtropical and perturbed-sym-

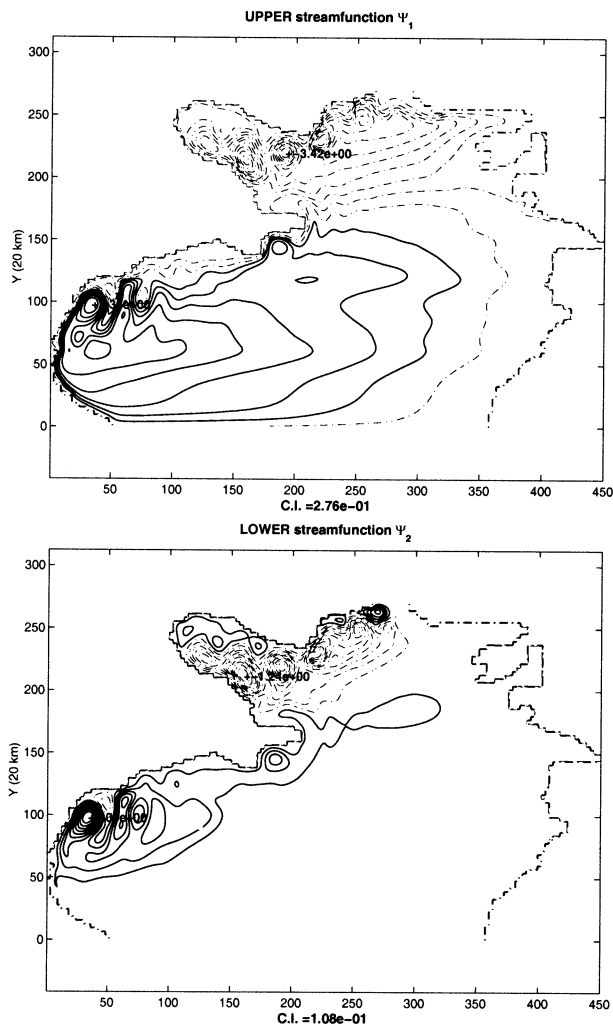


FIG. 15. As in Fig. 14a but for a realistic Hellerman and Rosenstein (1983) wind stress on a 20-km grid ( $T_0 = 90$  yr).

metric ones are connected to each other by a saddle-node bifurcation, but isolated from the subpolar branch. In section 5a we summarize the results of the present Part II and in section 5b we discuss the conclusions of the entire two-part paper.

### a. Summary

Part II aims at understanding the time-dependent behavior of the double-gyre circulation, with an emphasis on the causes of its low-frequency variability. Linear stability analysis and forward integration in time of the model were used. We first studied in detail the model's idealized version, within a  $2000 \text{ km} \times 1000 \text{ km}$  domain; in this model version, wind stress is purely zonal and has a sinusoidal profile in the meridional direction.

As the wind stress is intensified, each one of the three steady-state solution branches obtained in Part I (see Fig. 2 there) undergoes a Hopf bifurcation (see Figs. 1

and 2 here for the subpolar and subtropical branch). The time-dependent solutions obtained near the bifurcation points do exhibit periodic behavior with a period very close to that computed by the linear analysis. The growing oscillatory modes that lead to these limit cycles are mainly barotropic for all three branches (see again Figs. 1 and 2). The prevalence of barotropic modes is a very robust feature of the model's primary Hopf bifurcations in the main parameter range that we studied.

For other parameter ranges, though, baroclinic instabilities are also present (see Fig. 3). A decrease of  $H_2$ , that is, a decrease of the internal Rossby radius of deformation, favors baroclinic instabilities. In this case, the first Hopf bifurcation for the subpolar branch of solutions occurs before the saddle-node bifurcation (recall Fig. 6 of Part I; cf. also Dijkstra and Katsman 1997 and Ghil et al. 2002b).

The subtropical solutions have a more intense subtropical recirculation cell, while the area covered by the entire subtropical gyre is smaller than that of the subpolar one. A cascade of period-doubling bifurcations occurs along the subtropical branch soon after the first Hopf bifurcation (Fig. 4). The mode involved in this process is a subtropical, low-frequency gyre mode. Its amplitude and period increase regularly before the first period-doubling bifurcation. Afterward, the flow becomes rapidly chaotic until the trajectories in phase space touch the perturbed-symmetric branch, which is unstable (Fig. 5). The numerical evidence strongly suggests a homoclinic explosion that involves an infinite number of saddle-node, period-doubling and homoclinic bifurcations at a critical value of the wind stress intensity.

The subtropical solutions are subsequently attracted toward large-amplitude, low-frequency limit cycles that loop around the subpolar branch (Figs. 6 and 8); these subpolar limit cycles are the approximate mirror images of the ones spanned by oscillatory subtropical gyre modes (Fig. 9). The periodic solutions so obtained, however, are not generated by a Hopf bifurcation off the subpolar branch and their dynamical origin has not been pursued further.

The solutions that arise by primary and secondary Hopf bifurcation, at lower  $\sigma$  values, off the connected subpolar branch involve mainly resonant Rossby basin modes (Fig. 7) with periods of 4–5 months. These modes later on affect the low-frequency subpolar limit cycles, with periods of 2–3 yr (Fig. 10), by adding their higher-frequency variability.

At high wind stress forcing levels, vigorous oscillations of relaxation type, with an interdecadal timescale, predominate on the subpolar branch. They correspond to the slow growth of an energetic, nearly symmetric dipole, followed by its rapid destabilization and associated eddy generation. This behavior is associated with alternations between an extended and fairly straight eastward jet on the one hand and a short, meandering

one on the other (see also Ghil et al. 2002b, and references there).

For even higher forcing, the subpolar and subtropical dynamics may recombine: irregular transitions between the two types of (approximately) mirror-symmetric solutions are observed and each transition seems to be punctuated by the slow growth of a nearly symmetric dipole (Fig. 12). The numerical evidence here points to a second homoclinic bifurcation. This second bifurcation is associated with the subpolar branch and seems to connect subpolar trajectories with a fixed point that belongs to the perturbed-symmetric branch.

The reason for this behavior is the following: in exactly symmetric QG models, “figure-eight” homoclinic orbits may arise (Chang et al. 2001) and lead to a homoclinic explosion simultaneously for both asymmetric branches (Nadiga and Luce 2001). In the case of perturbed symmetry, like in the SW equations, this phenomenon is also perturbed in parameter space. The first homoclinic bifurcation occurs when limit cycles off the subtropical branch touch the perturbed-symmetric one. This is followed by a second one, as the phenomenon is approximately repeated for limit cycles that are associated with the subpolar branch. The parameter dependence of the time-dependent dynamics is summarized in Fig. 16.

In order to pursue the investigation in a slightly more realistic context, we performed a set of forward integrations in a rectangular domain that has roughly the size and aspect ratio of the North Atlantic basin between 20° and 60°N, and also in a domain that reproduces the shape of the eastern and western shores of the basin between these two latitudes. The latter simulation used an eddy-resolving 12-km grid and an eddy viscosity that is half the lowest one used by Berloff and McWilliams (1999;  $A = 200 \text{ m}^2 \text{ s}^{-1}$  here vs  $400 \text{ m}^2 \text{ s}^{-1}$  in their work).

Both of these more realistic model versions present three robust modes of variability with periodicities of 6–7 years, 3 years, and 20–25 months (see Figs. 13 and 14). The 6–7 year and the 20-month peaks agree fairly well with those exhibited by the variability of the Gulf Stream axis position, as deduced from 40 years of COADS data by Speich et al. (1995). The robustness of these spectral peaks seems to indicate that the shape of the basin is not a decisive factor for its low-frequency variability (see also Dijkstra and Molemaker 1999).

The separation and meandering of the Gulf Stream, as well as the size and strength of the subpolar versus the subtropical gyre, are much more realistic when using climatological wind stress forcing (see Fig. 15). A more realistic wind stress field, though, does not affect significantly the spatiotemporal variability patterns obtained throughout our study.

## b. Discussion

In the present paper, we have taken a number of steps in the direction of greater realism in applying the dy-

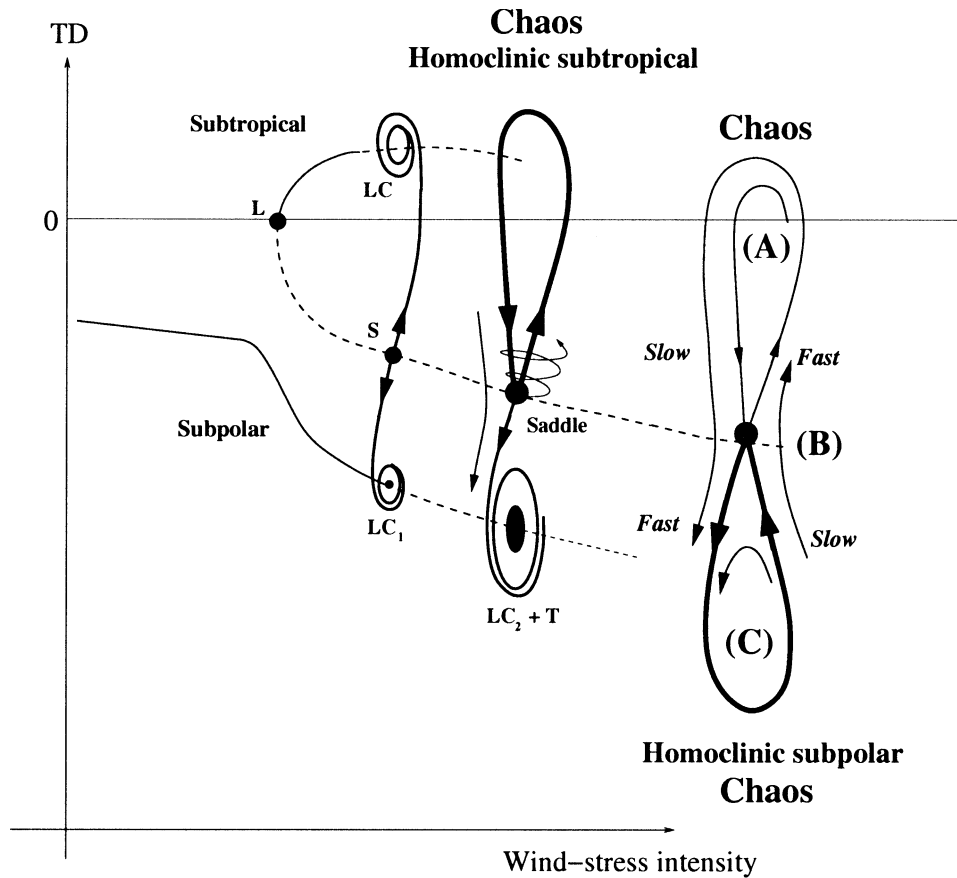


FIG. 16. Sketch of the local and global dynamics of the model's bifurcation tree, as a function of the wind stress intensity: LC stands for a subtropical limit cycle;  $LC_1$  and T represent the small-amplitude, high-frequency subpolar limit cycles, and the 2-tori of Fig. 7, respectively;  $LC_2$  corresponds to the large-amplitude, low-frequency, subpolar limit cycles of Fig. 9; L and S refer to the limit point (or turning point) at the origin of the subtropical and perturbed-symmetric branch, and the saddle-node point on the perturbed-symmetric branch, respectively; (A), (B), and (C) correspond to the flows in Fig. 12, while *Slow* and *Fast* refer to the phase-space speed of the trajectory for the relaxation oscillations associated with  $LC_2$ .

namical systems approach to the oceans' wind driven circulation. This approach appears successful in several respects and it points to the paramount importance of global bifurcations in determining the double-gyre circulation's low-frequency variability. The occurrence of one or even two successive homoclinic explosions leads to an intricate and rich interannual and interdecadal variability that only the most recent studies (Meacham 2000; Chang et al. 2001; Nadiga and Luce 2001) have started to elucidate. Many questions remain and we formulated several working hypotheses for their resolution.

A key question one may ask concerns the physical origin of these homoclinic bifurcations. The low-frequency oscillatory gyre modes are always involved in their appearance (see sections 3a and 3b). Their amplitude in the  $(E_p, E_k)$  plane grows as the system's energy is increased by a stronger wind stress. It is this growth that leads, essentially, to the subtropical homoclinic bifurcation. The more precise question: Why is there no other saturation mechanism for these modes?

Simonnet and Dijkstra (2002) pointed out the importance of the symmetry in the spontaneous generation of the oscillatory gyre modes. Their work indicates that the (perturbed) symmetric branch must be involved in the low-frequency relaxation oscillations that are associated with the nearby homoclinic orbits. There is, therefore, growing evidence for an underlying, essentially low-dimensional system that subsumes these three interrelated phenomena: (perturbed) pitchfork bifurcation, oscillatory gyre modes, and the homoclinic bifurcations that follow.

In our numerical simulations, including the most realistic, eddy-resolving, low-viscosity ones, we found a net separation in time and space scale between eddy fluctuations, on the one hand, and the energetic relaxation oscillations of the recirculation zone's dipolar structure, on the other. This suggests that the low-frequency behavior of the double-gyre circulation observed here is likely to survive in the much more turbulent regimes that can, finally, be obtained in the cur-

rent ocean GCMs (Chao et al. 1996; Smith et al. 2000). It is, however, unclear if the relaxation oscillations observed here will survive a flow regime that is dominated by baroclinic instabilities. No studies so far have considered the effect of the first baroclinic instabilities occurring before the pitchfork bifurcation on the first global bifurcations (after the pitchfork bifurcation).

The irregular transitions between subpolar and subtropical flow patterns that are induced by global bifurcations provide a rather simple, although still conjectural, explanation for the bimodality of the Kuroshio and the Gulf Stream (Schmeits and Dijkstra 2001). More generally, it will be interesting to confront a typical statistical approach to oceanic flows—patterned after those in use when studying atmospheric weather regimes and their Markov chains (Cheng and Wallace 1993; Kimoto and Ghil 1993a,b; Ghil and Robertson 2002)—with a dynamical systems one. In order to reconcile these two approaches, there is still a long way to fully understand how homoclinic bifurcations and (perturbed) symmetry affect the low-frequency variability of the double-gyre circulation in model configurations that include more realistic bathymetry, wind stress, and vertical resolution.

In particular, the dynamical origin of the 7-year peak observed in several simulations of the double-gyre circulation still remains an open question. Preliminary results point toward the residual influence of the oscillatory gyre modes after the first global bifurcation. If this result is confirmed by further studies, and if the spatiotemporal signature of these peak is the same as the one found in atmospheric and oceanic observations (Moron et al. 1998; Plaut et al. 1995; Simonnet 2001), it would provide a striking example of the importance of dynamical systems concepts in understanding mid-latitude oceanic variability.

*Acknowledgments.* It is a pleasure to thank H. A. Dijkstra, S. Jiang, and S. Speich for discussions and correspondence, and Z. Sirkes for the DAMEE-NAB bathymetry. ES's work was supported by a doctoral fellowship at the Université Paris-Sud, MG's by an NSF Special Creativity Award and NSF Grant ATM00-82131, and KI's by ONR Grant N00014-99-109920. Computations were carried out at Indiana University and IDRIS (France), with support from NSF Grant CDA-9601632 (RT). SW is supported in part by the Office of Naval Research under Grant N00014-96-1-0425 and by the National Science Foundation under Grant DMS-0072612.

#### REFERENCES

- Berloff, P. S., and S. P. Meacham, 1997: The dynamics of an equivalent-barotropic model of the wind-driven circulation. *J. Mar. Res.*, **55**, 407–451.
- , and J. McWilliams, 1999: Large-scale, low-frequency variability in wind-driven ocean gyres. *J. Phys. Oceanogr.*, **29**, 1925–1945.
- Chang, K.-I., K. Ide, M. Ghil, and C.-C. Lai, 2001: Transition to aperiodic variability in a wind-driven double-gyre circulation model. *J. Phys. Oceanogr.*, **31**, 1260–1286.
- Chao, Y., A. Gangopadhyay, F. O. Bryan, and W. R. Holland, 1996: Modeling the Gulf Stream system: How far from reality? *Geophys. Res. Lett.*, **23**, 3155–3158.
- Chassignet, E. P., and Coauthors, 2000: DAMEE-NAB: The base experiment. *Dyn. Atmos. Oceans*, **32**, 155–183.
- Cheng, X., and J. M. Wallace, 1993: Cluster analysis of the Northern Hemisphere wintertime 500-hPa height field: Spatial patterns. *J. Atmos. Sci.*, **50**, 2674–2696.
- Constantin, P., C. Foias, B. Nicolaenko, and R. Temam, 1989: *Integral Manifolds and Inertial Manifolds for Dissipative Partial Differential Equations*. Springer-Verlag, 122 pp.
- Dettinger, M. D., M. Ghil, C. M. Strong, W. Weibel, and P. Yiou, 1995: Software expedites singular-spectrum analysis of noisy time series. *Eos, Trans. Amer. Geophys. Union*, **76**, 12–21.
- Dijkstra, H. A., and C. A. Katsman, 1997: Temporal variability of the wind-driven quasi-geostrophic double gyre ocean circulation: Basic bifurcation diagrams. *Geophys. Astrophys. Fluid Dyn.*, **85**, 195–232.
- , and M. J. Molemaker, 1999: Imperfections of the North-Atlantic wind-driven ocean circulation: Continental geometry and asymmetric windstress. *J. Mar. Res.*, **57**, 1–28.
- Eckmann, J. P., 1981: Roads to turbulence in dissipative dynamical systems. *Rev. Mod. Phys.*, **53**, 643–654.
- Ghil, M., and S. Childress, 1987: *Topics in Geophysical Fluid Dynamics: Atmospheric Dynamics, Dynamic Theory and Climate Dynamics*. Springer-Verlag, 485 pp.
- , and A. W. Robertson, 2002: “Waves” vs. “particles” in the atmosphere’s phase space: A pathway to long-range forecasting? *Proc. Natl. Acad. Sci.*, **99** (Suppl.), 2493–2500.
- , and Coauthors, 2002a: Advanced spectral methods for climatic time series. *Rev. Geophys.*, **40**, 1003, doi:10.1029/2000RG000092.
- , Y. Feliks, and L. Sushama, 2002b: Baroclinic and barotropic aspects of the wind-driven double-gyre model. *Physica D*, **167**, 1–35.
- Guckenheimer, J., and P. Holmes, 1990: *Nonlinear Oscillations, Dynamical Systems and Bifurcations of Vector Fields*. 2d ed. Springer-Verlag, 453 pp.
- Hellerman, S., and M. Rosenstein, 1983: Normal monthly wind stress over the world ocean with error estimates. *J. Phys. Oceanogr.*, **13**, 1093–1104.
- Jiang, S., F.-F. Jin, and M. Ghil, 1995: Multiple equilibria, periodic, and aperiodic solutions in a wind-driven, double-gyre, shallow-water model. *J. Phys. Oceanogr.*, **25**, 764–786.
- Jin, F.-F., J. D. Neelin, and M. Ghil, 1994: El Niño on the Devil’s staircase: Annual subharmonic steps to chaos. *Science*, **264**, 70–72.
- , —, and —, 1996: El Niño/Southern Oscillation and the annual cycle: Subharmonic frequency-locking and aperiodicity. *Physica D*, **98**, 442–465.
- Kimoto, M., and M. Ghil, 1993a: Multiple flow regimes in the Northern Hemisphere winter. Part I: Methodology and hemispheric regimes. *J. Atmos. Sci.*, **50**, 2625–2643.
- , and —, 1993b: Multiple flow regimes in the Northern Hemisphere winter. Part II: Sectorial regimes and preferred transitions. *J. Atmos. Sci.*, **50**, 2645–2673.
- Kuznetsov, Y. A., 1995: *Elements of Applied Bifurcation Theory*. Springer-Verlag, 591 pp.
- Lee, T., and P. Cornillon, 1995: Temporal variation of meandering intensity and domain-wide lateral oscillations of the Gulf Stream. *J. Geophys. Res.*, **100**, 13 603–13 613.
- Legras, B., and M. Ghil, 1983: Ecoulements atmosphériques stationnaires, périodiques et aperiodiques. *J. Méc. Théor. Appl.*, Special Issue, *Two-Dimensional Turbulence*, R. Moreau, Ed., Gauthier-Villars, 45–82.
- Lin, R.-Q., F. Busse, and M. Ghil, 1989: Transition to two-dimensional

- turbulent convection in a rapidly-rotating annulus. *Geophys. Astrophys. Fluid Dyn.*, **45**, 131–157.
- Lions, J. L., O. P. Manley, R. Temam, and S. Wang, 1997: Physical interpretation of the attractor dimension for the primitive equations of atmospheric circulation. *J. Atmos. Sci.*, **54**, 1137–1143.
- Lorenz, E. N., 1963: The mechanics of vacillation. *J. Atmos. Sci.*, **20**, 448–464.
- Mann, M. E., and J. M. Lees, 1996: Robust estimation of background noise and signal detection in climatic time series. *Climatic Change*, **33**, 409–445.
- Meacham, S. P., 2000: Low-frequency variability in the wind-driven circulation. *J. Phys. Oceanogr.*, **30**, 269–293.
- Moron, V., R. Vautard, and M. Ghil, 1998: Trends, interdecadal and interannual oscillations in global sea-surface temperatures. *Climate Dyn.*, **14**, 545–569.
- Nadiga, B. T., and B. P. Luce, 2001: Global bifurcation of Shilnikov type in a double-gyre ocean model. *J. Phys. Oceanogr.*, **31**, 2669–2690.
- Plaut, G., M. Ghil, and R. Vautard, 1995: Interannual and interdecadal variability in 335 years of central England temperatures. *Science*, **268**, 710–713.
- Primeau, F. W., 1998: Multiple equilibria and low-frequency variability of wind-driven ocean models. Ph.D. thesis, Massachusetts Institute of Technology/Woods Hole Oceanographic Institution, 157 pp.
- Ruelle, D., and F. Takens, 1971: On the nature of turbulence. *Commun. Math. Phys.*, **20**, 167–192.
- Schmeits, M. J., and H. A. Dijkstra, 2001: Bimodality of the Gulf Stream and Kuroshio. *J. Phys. Oceanogr.*, **31**, 3435–3456.
- Sheremet, V. A., G. R. Ierley, and V. M. Kamenkovich, 1997: Eigenanalysis of the two-dimensional wind-driven ocean circulation problem. *J. Mar. Res.*, **55**, 57–92.
- Shilnikov, L. P., 1965: A case of the existence of a denumerable set of periodic motions. *Sov. Math. Dokl.*, **6**, 163–166.
- Simonnet, E., 1998: Some numerical problems related to geophysical flows. Ph.D. thesis, Université de Paris-Sud, Orsay, France, 154 pp.
- , 2001: Interannual and interdecadal variability in 120 years of daily SLP data: Links with other surface fields. INLN preprint, 26 pp.
- , and H. A. Dijkstra, 2002: Spontaneous generation of low-frequency modes of variability in the wind-driven ocean circulation. *J. Phys. Oceanogr.*, **32**, 1747–1762.
- , R. Temam, S. Wang, M. Ghil, and K. Ide, 1998: Successive bifurcations in a shallow-water ocean model. *Sixteenth International Conference on Numerical Methods in Fluid Dynamics*, C.-H. Bruneau, Ed., *Lecture Notes in Physics*, Vol. 515, Springer-Verlag, 225–230.
- , M. Ghil, K. Ide, R. Temam, and S. Wang, 2003: Low-frequency variability in shallow-water models of the wind-driven ocean circulation. Part I: Steady-state solutions. *J. Phys. Oceanogr.*, **33**, 712–728.
- Smith, R., T. Linda, E. P. Chassignet, and R. Bleck, 2000: The impact of lateral boundary conditions and horizontal resolution on North Atlantic water mass transformations and pathways in an isopycnic coordinate ocean model. *J. Phys. Oceanogr.*, **30**, 137–159.
- Speich, S., H. A. Dijkstra, and M. Ghil, 1995: Successive bifurcations in a shallow-water model applied to the wind-driven ocean circulation. *Nonlinear. Proc. Geophys.*, **2**, 241–268.
- Strong, C., F.-F. Jin, and M. Ghil, 1995: Intraseasonal oscillations in a barotropic model with annual cycle, and their predictability. *J. Atmos. Sci.*, **52**, 2627–2642.
- Temam, R., 1998: *Infinite-Dimensional Dynamical Systems in Mechanics and Physics*. 2d ed. Springer-Verlag, 500 pp.
- Tziperman, E., L. Stone, M. A. Cane, and H. Jarosh, 1994: El Niño chaos: Overlapping of resonances between the seasonal cycle and the Pacific ocean-atmosphere oscillator. *Science*, **264**, 72–74.